

UNIVERSITY OF LATVIA
FACULTY OF PHYSICS AND MATHEMATICS



Martins Zubkins

**DEVELOPMENT OF TRANSPARENT CONDUCTING ZnO
BASED FILMS DEPOSITION PROCESS AND FILMS
CHARACTERIZATION**

SUMMARY OF DOCTORAL THESIS

Submitted for the degree of Doctor of Physics
Subfield: Solid State Physics

Rīga, 2018

The doctoral thesis was carried out in Institute of Solid State Physics, University of Latvia from 2013 to 2017.

The thesis contains an introduction, 5 chapters with reference lists and 4 appendices.

Form of the thesis: dissertation in solid state physics.

Supervisor: *Dr. habil. phys.* **Juris Purāns**, senior researcher.

Reviewers:

1. *Dr. habil. phys.*, **Māris Knite**, professor, Riga Technical University
2. *Dr. phys.*, **Aleksandrs Kaļinko**, researcher, Universitat Paderborn
3. *Dr. chem.*, **Donāts Erts**, senior researcher, Institute of Chemical Physics, University of Latvia

The defence of the doctoral thesis will take place in an open session of the Promotion Council of Physics, Astronomy and Mechanics of the University of Latvia on the 10th of May, 2018, at 15:00 in the conference hall of the Institute of Solid State Physics, University of Latvia.

The doctoral thesis and its summary are available at the Library of the University of Latvia (19 Raina Blvd, Riga) and Latvian Academic Library (10 Rupniecibas Str, Riga).

Chairman of the Doctoral Committee _____ *Dr. habil. phys.* **Linards Skuja**

Secretary of the Doctoral Committee _____ **Laureta Buševica**

©University of Latvia, 2018

©Mārtiņš Zubkins, 2018

ISBN 978-9934-18-330-0

Abstract

Transparent conducting oxide (TCO) thin films are widely used in flat panel displays, light emitting diodes and thin-film solar cells. In order to develop the technologies more efficient and less expensive, there is great demand for new improved TCO materials. An important task is to develop and produce indium free TCO films due to the high price and toxicity of indium. Aluminium doped zinc oxide (AZO) is considered as a potential alternative to the most commonly used indium tin oxide (ITO). Although AZO is extensively studied and used as a TCO material, there is still a lack of understanding of the relationship between native and impurity type defects, and deposition conditions that effect optical and electrical properties of the films. In order to be able to use TCO films in transparent electronics, it is necessary to produce a high quality and stable *p*-type TCO material, since the most TCOs are *n*-type. In addition, the deposition process of TCO films should be suitable for the TCO integration into multi-layer structures and large-scale production.

In this study, *n*-type AZO and *p*-type ZnO:Ir and Zn-Ir-O thin films have been deposited by a reactive DC magnetron sputtering technique which is suitable for the deposition on large-area substrates. The films were characterized by XRF, XRD, XAS, SEM, Raman and FTIR spectroscopy, electrical conductivity, Hall effect, thermoelectric measurements and visible light transmittance and reflectance. The properties of the films were analysed depending on deposition parameters and composition.

During the study, the deposition process of the AZO films has been developed. The influence of an oxygen flow rate on the structure and properties of the AZO films has been established. The study demonstrates and explains the rapid change in the ratio of zinc and aluminium concentrations at a low oxygen flow. Low resistivity ($10^{-4} \Omega\text{cm}$) is obtained in the narrow oxygen flow range. The electrical activation of Al impurities and the structure of the films rapidly changes depending on the oxygen flow used in the reactive process. Due to this effect the rapid change of the free electron concentration and mobility occurs.

ZnO doping with iridium results in the degradation of a crystalline structure until the structure becomes completely amorphous in the Ir concentration range between 7 and 16 at.%. As a result of the Ir concentration change, the Ir ion charge state transition between +5 and +4 is observed. A new and intense band around 720 cm^{-1} has been detected in the Raman spectra of the ZnO:Ir and Zn-Ir-O thin films and may be attributed to the stretching mode of O_2^{2-} peroxide ions. By increasing the Ir concentration, there is a rapid increase of electrical conductivity and visible light absorption. In the Ir concentration range from 12.4 to 16.4 at.% there is the transition from *n*-type to *p*-type conductivity.

Contents

1. Introduction	6
1.1 Motivation	6
1.2 Aim of the study	6
1.3 Scientific novelty of the work	7
1.4 Author's contribution	7
2. Transparent conducting oxides (TCO)	8
2.1 Overview and state of the art	8
2.1.1 Electrical conductivity	8
2.1.2 Visible light transmittance	8
2.1.3 <i>p</i> -type TCO	9
2.2 Zinc oxide (ZnO)	9
2.3 ZnM_2O_4 and a-Zn-M-O	9
3. Reactive magnetron sputtering	11
3.1 Basic principles	11
3.2 Reactive process	11
4. Experimental methods	12
4.1 Thin film deposition	12
4.2 Characterization methods	12
4.2.1 Thickness measurements – profilometry	12
4.2.2 X-ray fluorescence (XRF)	12
4.2.3 X-ray diffraction (XRD)	12
4.2.4 X-ray absorption (XAS)	13
4.2.5 Scanning electron microscopy (SEM)	13
4.2.6 Fourier transform infra-red and Raman spectroscopy	13
4.2.7 UV-Vis-NIR transmittance and reflectance measurements	13
4.2.8 Electrical properties and Hall effect	13
4.2.9 Thermoelectric measurements	13
5. ZnO:Al (AZO) thin films	14
5.1 Deposition parameters	14
5.2 Composition	14
5.3 Structure	15
5.4 Electrical properties	16
5.5 Optical properties	18
5.6 Summary and conclusions	21
6. ZnO:Ir and Zn-Ir-O thin films	22
6.1 Deposition parameters	22
6.2 Composition	22
6.3 Structure	23
6.3.1 X-ray diffraction measurements (XRD)	23

6.3.2	X-ray absorption measurements (XAS)	24
6.3.3	Surface morphology	26
6.3.4	Vibrational properties (FTIR and Raman measurements)	26
6.4	Electrical properties	30
6.5	Optical properties	32
6.6	Summary and conclusions	33
	Main thesis	34
	Bibliography	35
	Author's publication list	40
	Participation in conferences	40
	Participation in schools	41
	Acknowledgements	42

1. Introduction

1.1. Motivation

Transparent conducting materials play an important role in information technologies and power industry [1]. Fig. 1.1.1 summarizes the technologies, which require the transparent conducting materials and could be used to equip, for example, a vehicle. Visible light transmittance and electrical conductivity are simultaneously obtainable for the several material classes – transparent conducting oxide (TCO) thin films [2], thin (≈ 10 nm) metal layers, TCO/metal/ TCO structures [3, 4, 5], periodic metal grids [6, 7, 8], metal nanowire and carbon nanotube networks [9, 10, 11, 12], graphene [13, 14, 15, 16], and conductive polymer films [17].

The role of limited TCO properties gradually increases on the TCO containing devices as they become more complex. For example, to increase device performance it is necessary to increase the electrical conductivity of a transparent electrode. The accessibility of qualitative *n*- and *p*-type TCO materials that could be used as active elements is necessary for the development of transparent electronics. In order to improve the properties of existing materials or create the new TCO films, there is a need for the in-depth knowledge of the fundamental principles of TCOs.

Tin indium oxide ($\text{In}_2\text{O}_3:\text{Sn}$ – ITO) is the most commonly used material from the TCO class because it has unique electrical and optical properties [1, 2]. However, its toxicity and a high price stimulate the search of indium free materials. For this purpose, aluminum doped zinc oxide ($\text{ZnO}:\text{Al}$ – AZO) is widely investigated and used as a transparent electrode. AZO is a promising TCO material but it has not yet fully replaced ITO. The relationship between impurities, electrical properties and manufacturing methods are not yet fully understood [19, 20].

Although ZnO is a promising *n*-type TCO material, it is still problematic to produce a stable *p*-type transparent thin film and a *p-n* junction based on ZnO [21]. This is an obstacle to the full use of ZnO in electrical equipment. It has been found that the polycrystalline ZnIr_2O_4 films are transparent *p*-type semiconductors [22]. In addition, this material retains the properties also in an amorphous phase [23, 24], which is a technological advantage, since it is not necessary to use a high deposition temperature. However, this material has not yet been sufficiently investigated. The atomic structure and the sources of spontaneous *p*-type conductivity are still not well understood.

1.2. Aim of the study

The research object of this study is *n*- and *p*-type transparent and conductive thin films based on ZnO. The aim of the study is to develop thin films deposition process and investigate films physical



Figure 1.1.1. A vehicle equipped with the potential technologies which require transparent conducting materials [18].

properties to evaluate the possibility to use these films as transparent conductive materials. The films deposition technique is reactive magnetron sputtering. AZO films were selected as an *n*-type conductive material. Iridium doped ZnO and Zn-Ir-O films were selected as *p*-type conductive materials.

Objectives of the study:

- develop thin film deposition process and deposit transparent conductive films based on ZnO;
- investigate the composition, structure, electrical and optical properties of the thin films.

1.3. Scientific novelty of the work

The change of Al concentration in the AZO films by changing the oxygen flow during the reactive magnetron sputtering is demonstrated for the first time. The phenomenon is attributable to the desorption of non-oxidized zinc atoms from growing films surface at certain substrate temperature.

The set of ZnO films with Ir content varied in the large concentration range was deposited and characterized for the first time. The structure and properties of the films were investigated as a function of Ir concentration. The films with the corresponding composition have never been deposited by reactive magnetron sputtering. The local structure and vibrational properties were studied using X-ray absorption, Fourier-transform infrared (FTIR) and Raman spectroscopies. These methods have never been used to investigate Zn-Ir-O films and gave the new information about the compound. In addition, the transition between *n*- and *p*-type conductivity was observed by changing the Ir concentration in the films. The amorphization of the ZnO structure with the Ir concentration gave the new information about an amorphous ZnO phase, which is difficult to obtain and little studied.

1.4. Author's contribution

The contribution of the author:

- thin films deposition (ZnO, AZO, ZnO:Ir, Zn-Ir-O, IrO₂ and Al₂O₃) with magnetron sputtering;
- X-ray fluorescence (XRF) measurements;
- visible light transmittance and reflectance measurements;
- electrical conductivity and Hall effect measurements;
- thickness measurements with profilometer;
- processing and analysis of the results.

The results are published in 4 scientific papers and presented in 5 national and 9 international conferences. The author is the corresponding author of all scientific papers. During the study the author participated in 3 international schools.

2. Transparent conducting oxides (TCO)

2.1. Overview and state of the art

Transparent conducting oxide (TCO) thin films are materials that have attracted great attention, because they have unique and very useful properties – high visible light transmittance and electrical conductivity simultaneously. The resistivity of the TCO films is in the order of 10^{-4} Ωcm , which is only one to two orders of a magnitude higher than metals ($\rho_{Cu} = 1.7 \mu\Omega\text{cm}$, $\rho_{Sn} = 11 \mu\Omega\text{cm}$, $\rho_{Ti} = 42 \mu\Omega\text{cm}$). Optical transmittance in the visible light range is over than 80 %. Due to the mentioned properties, the TCO films are effectively used as transparent electrodes in both information technologies (flat panel displays – LCD, plasma displays, ELD, OLED and touch screens) and power industry (thin film solar cells, low-e windows, solar thermal collectors) [25]. The TCO films are also used as an active element in thin-film transistors, UV LEDs, detectors and gas sensors [26].

Visible light transmittance together with electrical conductivity can be obtained in the metal oxide thin films by creating shallow donor or acceptor defect levels in the wide band gap ($E_g > 3.1$ eV). *N*-type polycrystalline TCO thin films ($\text{In}_2\text{O}_3:\text{Sn}$ – ITO, $\text{ZnO}:\text{Al}$ – AZO un $\text{SnO}_2:\text{F}$ – FTO), *n*-type amorphous indium-based active semiconducting oxides (ASO) and copper containing polycrystalline *p*-type thin films with a delafossite structure (CuMO_2) are sufficiently developed and available. The development of indium-free TCO and ASO, the production of stable and high-quality *p*-TCO and epitaxially grown TCO films are the main trends in the field of transparent conducting oxides.

2.1.1. Electrical conductivity

The resistivity of In_2O_3 , ZnO and SnO_2 is very high ($\gtrsim 10^7 \Omega\text{cm}$) if the compounds are stoichiometric or without proper dopants. High *n*-type conductivity at room temperature can be obtained by creating shallow donor type defects that promote the generation of charge carriers in the conductive band. The lattice defects as oxygen vacancies, interstitial protons and proper substitutional defects efficiently produce excess of electrons in the vicinity of the defect. If the electron orbits sufficiently overlap, then the electron delocalizes in the vicinity of the defect and fills the free energy levels at the bottom of the conduction band [27]. At certain electron concentration Fermi level shifts in to the conduction band and the semiconductor becomes degenerated with metallic conductivity.

The conductivity can be further enhanced by increasing the mobility of electrons. The mobility is inversely proportional to the effective mass of electrons. The orbital overlap between metal cations and oxygen anions strongly affects the electron mobility in the TCO films. In general the effective mass of electrons is smaller if the *s*-orbitals of cations are predominant in the conduction band.

In the crystal volume there are several scattering mechanisms like scattering of lattice phonons (optical and acoustic), neutral and ionized impurities, dislocations and electron-electron scattering. In the polycrystalline material the additional scattering of grain boundaries occurs. The contribution of each scattering mechanism is strongly influenced by the concentration of impurities and temperature. In the strongly degenerated polycrystalline TCO films the main scattering mechanisms are scattering of ionized impurities, acoustic phonons and grain boundaries [28].

2.1.2. Visible light transmittance

A material interacts with light in three different ways – transmits, reflects or absorbs the electromagnetic energy. The processes depend on the complex optical constants of the material, which in turn depend on a light frequency. The visible light transmittance is defined as the intensity ratio of incident and transmitted light in the range approximately from 400 to 700 nm.

The transmittance is determined by two spectral regions that are opaque due to the different interaction between the light and material.

Fundamental absorption is dominant at short wavelengths ($\lambda < \lambda_{gap}$), since photon energy is greater than a band gap and is absorbed by the electronic transition between zones. The optical band gap larger than 3.1 eV provides low absorption in the visible light range. At long wavelengths ($\lambda > \lambda_p$) the light is reflected due to free electron oscillations described by the Drude free electron model [29].

2.1.3. *p*-type TCO

Most of the commercially available TCO films are *n*-type. Several potential applications of the TCO films are still limited since it is difficult to produce these oxides with *p*-type conductivity [30, 31, 32]. High quality *p*-TCO in the combination with *n*-TCO could be used in transparent electronics as a *p-n* junction.

The electronic structure of metal oxides is responsible for the problem of obtaining *p*-type conductivity. The top of the valence band is formed of localized and anisotropic O $2p$ electron orbitals [33]. As the result, the oxide exhibits hopping conductivity together with low hole mobility due to the large effective mass [34]. The energetic deep O $2p$ orbitals make it difficult to create shallow acceptor levels and obtain *p*-type conductivity.

A widely used strategy is to use the cations with filled *d* or *s* shells, which are close to the top of the valence band, for the production of *p*-type metal oxides. The hybridization of O $2p$ orbitals occurs after an interaction with the filled cation orbitals. As the result, the curvature of the valence band increases, which reduces the effective mass of holes. The large curvature of the valence band alone does not provide the *p*-type conductivity, because it is also necessary to create holes in the valence band. Acceptor type defects, which can be either native defects or impurities, must have low formation energy. The levels of the acceptor defects should be sufficiently shallow to make it easy to activate holes in the valence band. Along with the Fermi level shift in the direction of the valence band the spontaneous formation of compensation defects should be avoided.

2.2. Zinc oxide (ZnO)

ZnO crystallizes in the thermodynamically stable hexagonal wurtzite-type structure $P6_3mc$ (No. 186) in environmental conditions. The structure has a unit cell with two lattice parameters *a* and *c*. Zinc atom is located in ZnO_4 tetrahedra, which are connected together through the corners. Atoms in the tetrahedron are coupled with sp^3 covalent bonds, but they also have a pronounced ionic character. ZnO is a semiconductor with a wide (≈ 3.4 eV) and direct band gap in the center of the Brillouin zone Γ ($k = 0$) [35]. The top of the valence band are predominantly formed of O $2p$ orbitals, but the bottom of the conduction band of Zn $4s$ orbitals [36].

ZnO films without native or impurity type defects are electrical insulators. With controlled doping, ZnO can be transformed into a semiconductor or even into an oxide with metallic conductivity, maintaining the visible light transmittance. ZnO has a strong tendency to naturally formed as an *n*-type semiconductor. In order to obtain high *n*-type conductivity, ZnO is most commonly doped with the elements from IIIB group (Al, Ga, In), which should replace the Zn cations in the lattice. The *p* electron from the outer shell of dopant does not need to form a bond and it can be thermally excited in the conduction band.

2.3. ZnM_2O_4 and *a-Zn-M-O*

The relatively new and different class of *p*-type TCOs is the spinels ZnM_2O_4 ($M = Co, Rh, Ir$) [37]. ZnM_2O_4 crystallizes in the cubic spinel structure with the space group $Fd-3m$ (No. 227) [38]. Zn is connected with four O atoms in tetrahedral coordination, but *M* with six O atoms in octahedral coordination [39, 40]. The electronic structure of ZnM_2O_4 is characterized by large *M* *d*-level splitting in the strong octahedral ligand field. Due to the strong field, the *d*-levels split into completely filled t_{2g}^6 levels ($d_{xy}, d_{yz},$ and d_{zx}) and completely empty e_g^0 (d_z^2 and $d_{x^2-y^2}$) levels [37, 41]. Therefore, the d^6 shell of transition metal ions ($Co^{3+}, Rh^{3+},$ and Ir^{3+}) can be considered

as quasi-filled and it interacts with O 2*p* orbitals.

Polycrystalline thin films of ZnIr₂O₄ that are deposited without intentional doping are transparent (60 % at 550 nm) *p*-type semiconductors ($\sigma = 3.4 \text{ Scm}^{-1}$, $E_{\text{g}}^{\text{opt}} = 2.97 \text{ eV}$) [22]. ZnIr₂O₄ is a thermodynamically metastable phase in which cation vacancies (V_{Zn} and V_{Ir}) and substitutional (Zn_{Ir}) defects have the lowest formation energies between the native defects [42]. These defects act as shallow acceptors and could be responsible for the spontaneous *p*-type conductivity [40, 42]. The structure of ZnIr₂O₄ is isotropic and the local structure of the crystalline phase remains also in the amorphous state.

3. Reactive magnetron sputtering

3.1. Basic principles

Magnetron sputtering is a physical vapour deposition technique, which is widely used in scientific laboratories and in the production of industrial coatings. This method is suitable for the large-scale production of thin films, because it is possible to deposit high-quality homogeneous films on large substrates with a relatively high deposition rate. Magnetron sputtering is the most commonly used technique of TCO films deposition for transparent electrode applications [43].

Thin films are deposited in the glow discharge (plasma) process. The principle of magnetron sputtering is shown in Fig. 3.1.1. A chamber is pumped to a high vacuum ($\sim 10^{-6}$ Torr) to reduce the concentration of impurities in the thin films. Then inert gas (working gas) is continuously injected into the chamber and pumped out continuously in order to provide constant pressure. Plasma is obtained by applying a negative voltage to the cathode (target) in order to ionize the inert gas atoms. The positive gas ions accelerate in the direction of the target and sputter the target atoms (mostly neutral) and secondary electrons that are important for the plasma maintenance. Magnets are located below the target, generating a magnetic field perpendicular to an electric field that localizes the electrons around the magnetic field lines and provides efficient inertial gas ionization near the target surface. Sputtered atoms from the target material condense on a substrate and form a thin film. The effectiveness of sputtering is characterized by the average number of sputtered target atoms per one ion incident (sputtering yield).

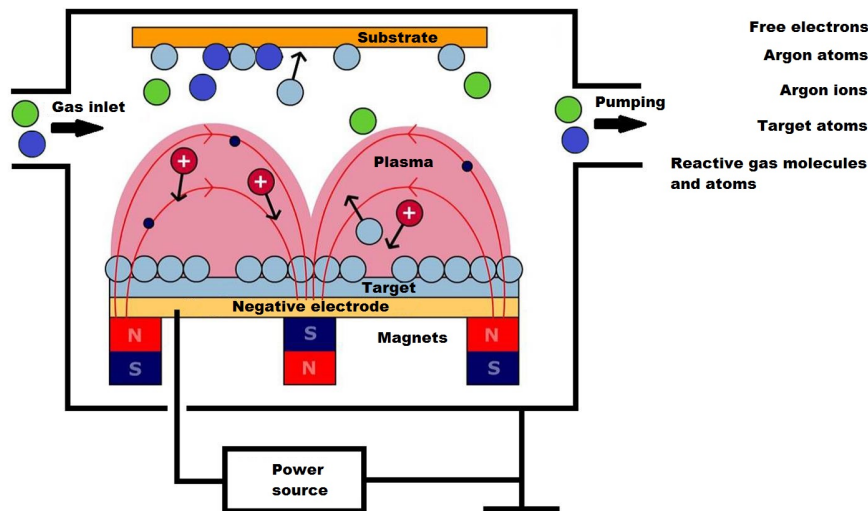


Figure 3.1.1. Magnetron sputtering.

3.2. Reactive process

Reactive sputtering is required in order to deposit different compound (e.g. oxides or nitrides) thin films from a metal target. In this process, the metal target is sputtered in an argon and reactive gas (RG), such as oxygen or nitrogen, atmosphere. The RG reacts with sputtered target atoms on the substrate surface and forms a compound. The chemical composition of the film, thus – the properties of the film, could be controlled by adjusting the partial pressure of the RG. The reactive sputtering requires precise process control, since desired properties are often obtained only in the narrow range of RG partial pressure. The addition of the RG causes the stability problems of the process, as the compound also forms on the target surface [43].

4. Experimental methods

4.1. Thin film deposition

In this study, the thin films were deposited with the magnetron sputtering system Sidrabe G500M (Fig. 4.1.1). Before the deposition process, the vacuum chamber was pumped to base pressure $p_{base} < 1 \times 10^{-5}$ Torr using a Pfeiffer Vacuum HiPace 1800 turbo-pump and a Pfeiffer Vacuum DUO 65M rotary vane pump. The system is equipped with two rectangular magnetrons, which are cooled with water. Target dimensions are 145 mm \times 92 mm \times 3 mm. Argon (99.99 %) was used as a working gas, while oxygen (99.5 %) as a reactive gas in the deposition process of oxide films. Gas inlet was provided with mass flow controllers MKS 2179B and a multichannel control unit MKS 647C. The working pressure was adjusted by a gate valve VAT 64246-PE52 and a control unit VAT PM-5. The magnetrons were driven by a dual-channel power supply Melec SIPP2000USB. A substrate temperature of 300 °C was obtained by a self-made substrate heater.

4.2. Characterization methods

The composition, structure, optical and electrical properties of the thin films were studied by X-ray fluorescence (XRF), X-ray diffraction (XRD), X-ray absorption (XAS), Infrared Fourier (FTIR) spectroscopy, Raman spectroscopy, optical spectrophotometry, profilometry, electrical conductivity measurements, Hall effect and thermoelectric measurements.

4.2.1. Thickness measurements – profilometry

The thickness of the films was measured by a profilometer Dektak 150.

4.2.2. X-ray fluorescence (XRF)

The composition of the films was analyzed by an Eagle III XRF spectrometer using a Rh X-ray lamp and a nitrogen-cooled Si detector. Due to the difficulty of detecting elements that are lighter than sodium, the composition of oxide films is presented without an oxygen component.

4.2.3. X-ray diffraction (XRD)

The structure was examined by an X-ray diffractometer PANalytical XPert Pro with Cu $K\alpha$ radiation. The maximum power 2.2 kW, voltage 60 kV, accuracy 0.1° and instrumental broadening 0.06°. The Crystallography Open Database was used to identify different structural phases [44].



Figure 4.1.1. Vacuum sputter system Sidrabe G500M.

4.2.4. X-ray absorption (XAS)

The Zn K-edge (9659 eV) and Ir L₃-edge (11215 eV) X-ray absorption spectra (XAS) were measured in transmission mode at the SOLEIL synchrotron bending-magnet beamline Samba [45] in ambient conditions. The beamline is equipped with a sagittal focusing Si(220) monochromator and two Pd-coated collimating/focusing mirrors. The mirrors have been used to remove X-ray harmonics. The beam intensity was measured using three ionization chambers filled with argon and krypton gas. The samples were optimized by making the stack of thin films, simultaneously sputtered on polyimide tape, in order to achieve the best sample homogeneity and thickness.

4.2.5. Scanning electron microscopy (SEM)

The morphology and microstructure of the films was studied by SEM Lyra Tescan. The amplification of 50 to 200 thousand times was obtained using an electron accelerating voltage of 10 to 25 kV.

4.2.6. Fourier transform infra-red and Raman spectroscopy

The Fourier transform infra-red (FTIR) absorbance spectra were measured by using a VERTEX 80v vacuum FTIR spectrometer. The experiments were performed in the range from 60 to 8000 cm⁻¹, with the interferometer working in vacuum and with a resolution of 4 cm⁻¹.

Raman scattering spectroscopy measurements were carried out at room temperature using a SPEX1403 monochromator with multichannel detectors and an inVia Renishaw Raman microscope. The experimental resolution was 5 cm⁻¹. An Ar laser (514.5 nm) and YAG second harmonics laser (532 nm) were used as the excitation source. The incident beam power was about 5 mW.

4.2.7. UV-Vis-NIR transmittance and reflectance measurements

The transmittance and reflectance of the films in the range from 200 to 1100 nm were measured by a double-beam spectrophotometer Analytik Jena AG Specord 210. The measurements from 300 to 2500 nm were ordered at GroGlass Ltd.

4.2.8. Electrical properties and Hall effect

The temperature dependant conductivity, carrier concentration and mobility was measured in the Van der Pauw configuration from 90 to 330 K by using a Hall effect system HMS5000. Ohmic contacts were added in the corners of square shaped samples.

4.2.9. Thermoelectric measurements

In-plane Seebeck coefficient measurements were made by a self-assembled measurement system. Copper contact lines were thermally evaporated on the top of the films using shadow masks. The distance between the Cu lines was 2 mm and the length was 8 mm. The temperature difference was measured with two K-type thermocouples pressed to the ends of the Cu lines. The temperature was controlled with two Peltier elements and a Stanford Research Systems Temperature PTC10 temperature controller. The Seebeck voltage was measured with a Keithley 2128 nanovoltmeter.

5. ZnO:Al (AZO) thin films

5.1. Deposition parameters

AZO thin films were deposited on glass substrates by reactive DC magnetron sputtering from metal alloy target ZnAl (98:2 wt.%) at the constant power of 100 W. The films were deposited at different oxygen flow values - 1.0 (AZO1.0), 1.5 (AZO1.5), 2.0 (AZO2.0), 2.3 (AZO2.3), 2.5 (AZO2.5), 3.0 (AZO3.0) un 4.5 sccm (AZO4.5). The argon flow of 50 sccm was kept constant. The working pressure of 20 mTorr was adjusted using a gate valve. The substrates were heated approximately up to a temperature of 280 °C. Deposition time was 20 min and the distance between the target surface and substrate was 5 cm.

The thickness of the films is in the range between 134 and 475 nm (Fig. 5.1.1), although the deposition time of all samples was the same. Above $Q(O_2) = 3.0$ sccm, the deposition rate decreases slightly, because the target surface becomes more oxidized and the sputtering rate drops. The rapid decrease of the sputtering rate is observed below the $Q(O_2)$ of 2.0 sccm.

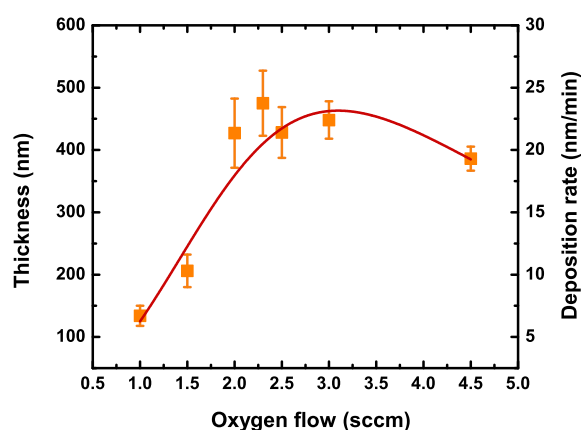


Figure 5.1.1. Thickness and deposition rate as a function of the $Q(O_2)$.

5.2. Composition

Intense Zn $K\alpha$ (8.6 keV) and Zn $K\beta$ (9.6 keV) fluorescence lines were detected in the XRF spectra of the AZO films. The magnitude of the Zn $K\alpha$ line decreases rapidly of the samples prepared with the $Q(O_2)$ below 2.0 sccm (Fig. 5.2.1(a)). This can be explained by the desorption of non-oxidized Zn atoms from the growing film surface during the deposition [46]. If the amount of oxygen in the process is insufficient, then the Zn atoms on the substrate are not completely oxidized. The substrate temperature in this case was sufficiently high (≈ 280 °C) to enhance the desorption of non-oxidized Zn. It also explains the decrease of deposition rate at low $Q(O_2)$ values.

The intensity of the Al $K\alpha$ (1.5 keV) fluorescence line is close to a noise level if the $Q(O_2)$ is above 2.0 sccm. It rapidly increases of the samples prepared with the $Q(O_2)$ below 2.0 sccm (Fig. 5.2.1(b)) indicating the sharp increase of the Al concentration in the films. It can be concluded that there is no significant Al desorption in the corresponding $Q(O_2)$ range if the substrate temperature is 280 °C. This can be explained by the fact that Al oxidizes more easily than Zn. In addition, Al vapor pressure is lower than that of Zn at the corresponding temperature [43].

The set of Al_2O_3 films with a varied thickness was deposited to determine the Al concentration in the AZO films. The Al $K\alpha$ line intensity in the Al_2O_3 films is linearly dependant on the thickness. Using this relationship, it was possible to calculate the Al concentration in the AZO films (Fig. 5.2.1(b)). The calculated Al concentration above the $Q(O_2)$ of 2.0 sccm is in the range from 1.0 to 4.0 at.%. The Al concentration rapidly grows when the $Q(O_2)$ is decreased

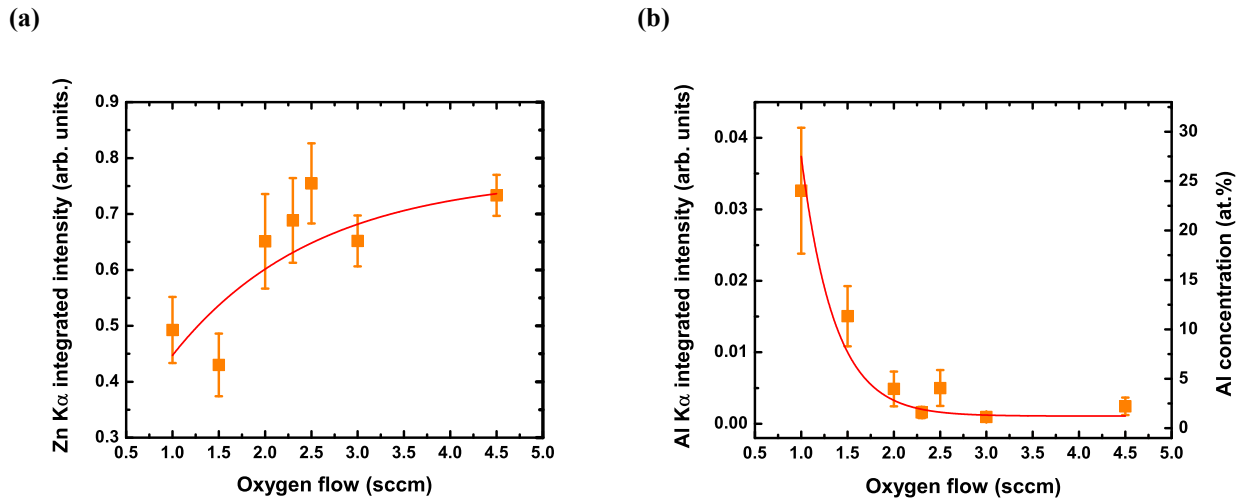


Figure 5.2.1. Zn $K\alpha$ līnijas integrētās intensitātes atkarība no $Q(O_2)$ (a). Al $K\alpha$ līnijas integrētās intensitātes un Al koncentrācijas atkarība no $Q(O_2)$ (b).

below 2.0 sccm.

5.3. Structure

The normalized XRD patterns of the AZO films are shown in Fig. 5.3.1. The films structure is X-rays amorphous if the $Q(O_2)$ is below 2.0 sccm. This is due to the lack of oxygen to form a stoichiometric ZnO compound and the increase of Al concentration with the possible formation of Al_2O_3 or $ZnAl_2O_4$ phases. Due to the desorption of non-oxidized Zn atoms, a crystalline Zn metal structure which is expected at a low oxygen flow [47, 48] is not detected.

The films crystallize in a hexagonal wurtzite-type structure (w-ZnO) if the $Q(O_2)$ is above 2.0 sccm. The diffraction maximum which corresponds to the (002) plane is the only intense one, indicating that crystallites are orientated with the c -axis perpendicular to the substrate surface. The spontaneous orientation of the crystallite in the direction of c -axis is thermodynamically favourable and is characteristic for w-ZnO films even on the glass substrates [50, 51]. This can be explained by the fact that the (001) plane has the lowest surface free energy [52]. The (101) maximum with a low intensity is observed for the samples deposited in the oxygen flow range from 2.0 to 2.5 sccm. The degree of preferred (002) orientation increases with the oxygen flow rate. No crystalline Zn, Al, Al_2O_3 or $ZnAl_2O_4$ phases were detected in any of these samples, which indicate a sufficient oxygen flow and the effective substitution of Zn^{2+} with Al^{3+} in the ZnO crystalline lattice. However, the

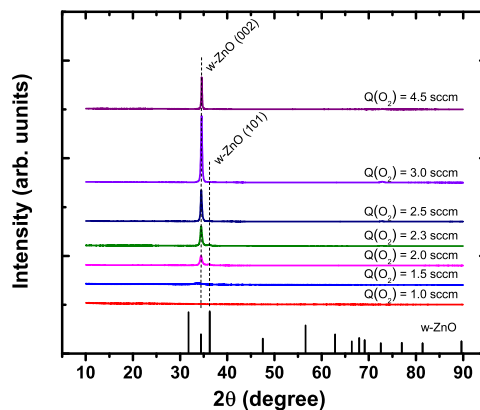


Figure 5.3.1. X-ray patterns of the AZO films and the reference of w-ZnO [49].

formation of amorphous or nanocrystalline Al_2O_3 and ZnAl_2O_4 phases can not be excluded.

The intensity of the (002) maximum increases with the oxygen flow rate indicating the improvement of crystallization. The intensity reaches the maximum value at $Q(\text{O}_2) = 3.0$ sccm and starts to decrease when the oxygen flow is further increased. It is possible to accurately control films stoichiometry by adjusting an oxygen flow rate. ZnO with the excess or deficit of Zn could be obtained if deposition takes place either in a metallic or highly oxidizing sputtering mode, respectively [48]. In this study, a high Zn deficit at a low $Q(\text{O}_2)$ is unlikely due to the desorption of non-oxidized Zn. An intense (002) maximum indicates a near-stoichiometric ZnO thin film [53]. The stoichiometry of the AZO films improves together with the effective substitution of Zn^{2+} with Al^{3+} when the $Q(\text{O}_2)$ is increased up to 3.0 sccm. The further increase of the $Q(\text{O}_2)$ creates a non-stoichiometric compound with oxidized Al impurities (Al_2O_3), which obstruct the crystallization of w-ZnO structure.

Energetic plasma particles that bombard the surface of growing film affect the crystallization process and microstructure [54]. The crystallization can be stimulated or interrupted depending on the energy of these particles. It is known that in the reactive process, negative oxygen ions, which are created on the surface of a target and accelerated in the direction of a substrate, strongly influence the growth of a film [55]. The energy of O^- depends on a cathode voltage and $Q(\text{O}_2)$ [56]. At the higher $Q(\text{O}_2)$ the cathode potential decreases, hence the energy of O^- .

The size of the crystallites grows from 5.2 to 55.5 nm when the oxygen flow is increased from 1.5 to 4.5 sccm. The diffraction angle (2θ) of the (002) maximum is slightly shifted compared to the w-ZnO crystal value of 34.42° [49]. This can be explained by an internal stress caused by the mismatch between the film and substrate surface, Al impurities, and point defects. The lattice constant c decreases from 5.31 to 5.18 Å (w-ZnO – 5.21 Å [49]) if the oxygen flow is increased from 1.5 to 4.5 sccm. The constant c of AZO1.5 is significantly higher (5.31 Å) compared to the w-ZnO crystal value. This result correlates with the literature data of films with high Al concentrations (19 – 48 at.%) [57].

The surface morphology of AZO2.5 and AZO3.0 and the cross-section SEM image of AZO4.5 are shown in Fig. 5.3.2.

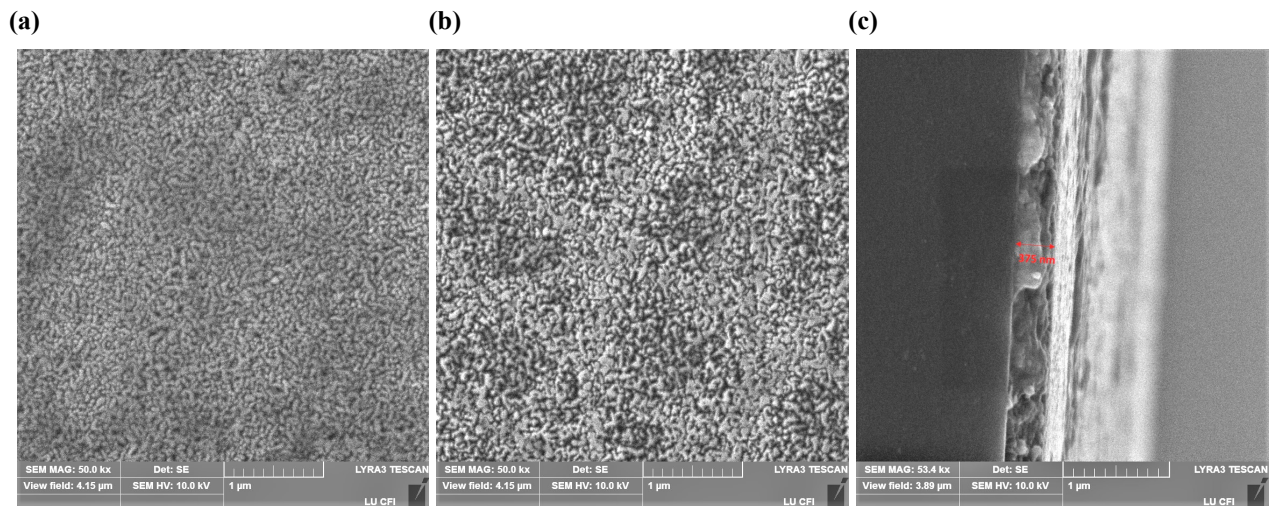


Figure 5.3.2. Surface morphology of AZO2.5 (a) and AZO3.0 (b). Cross-section SEM image of AZO4.5 (c).

5.4. Electrical properties

The electrical resistivity, charge carrier concentration and Hall mobility of the AZO films measured at a temperature of 300 K are shown in Fig. 5.4.1. High electrical conductivity is obtained in a narrow $Q(\text{O}_2)$ range with the minimum resistivity of $7.6 \times 10^{-4} \Omega\text{cm}$ of sample AZO2.3 (Fig. 5.4.1(a)). The higher conductivity is obtained in the samples with a lattice parameter c close to the

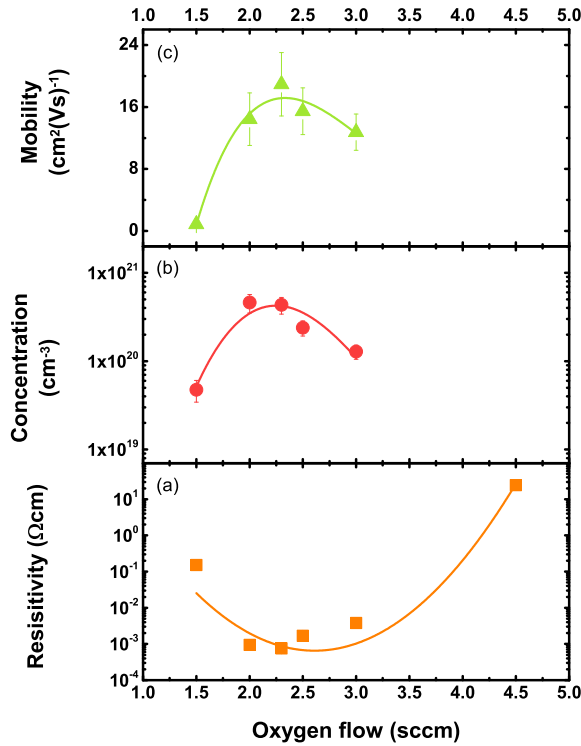


Figure 5.4.1. Resistivity (a), charge carrier concentration (b) and Hall mobility at a temperature of 300 K as a function of oxygen flow.

w-ZnO crystal value, indicating an effective incorporation of Al in the ZnO structure. The charge carrier concentration is $4.6 \times 10^{20} \text{ cm}^{-3}$ and the mobility is $18.8 \text{ cm}^2\text{V}^{-1}\text{s}^{-1}$ in sample AZO2.3 (Fig. 5.4.1(b,c)). The charge carrier concentration and mobility reduces when the $Q(\text{O}_2)$ is either increased or reduced. There are no Hall effect measurement data for sample AZO4.5 because the Hall voltage was not large enough to be able accurately detect it. The resistivity of sample AZO1.0 was too high to be measured. The sign of the Hall coefficient of all measured samples was negative, indicating *n*-type conductivity and free electrons in the conduction band as charge carriers.

Al impurities must replace Zn atoms in the ZnO crystal lattice to be an effective electron donor. In that case one additional electron from the shallow donor level could be excited in the conductive band. The decrease of the electron concentration in AZO1.5 film can be explained by the high Al concentration (Fig. 5.2.1(b)). In the case of high Al concentration the formation of non conductive Al_2O_3 or ZnAl_2O_4 phases is possible, which leads to the decrease of free electron concentration [58]. The decrease of electron concentration at higher $Q(\text{O}_2)$ values is caused by the oxidation of Al impurities (Al_2O_3). In this case the Al impurities no longer performs as a donor-type defect [59]. The increase of oxygen content in the sputtering atmosphere reduces also the concentration of interstitial zinc defects, which are donor-type defects in ZnO. At higher $Q(\text{O}_2)$ values the formation of zinc vacancies and interstitial oxygens, which could act as acceptor-type defects, is possible [60]. It is possible to calculate the percentage of electrically activated Al impurities if the concentration of free electrons and Al impurities is known. The highest Al activation of $\approx 56\%$ is obtained in sample AZO2.0.

Scattering mechanisms must be considered to interpret the effect of $Q(\text{O}_2)$ on electron mobility. In polycrystalline ZnO the grain barrier scattering is dominate if the electron concentration is in the range approximately from 1×10^{18} to $2 \times 10^{20} \text{ cm}^{-3}$ [61]. Above $2 \times 10^{20} \text{ cm}^{-3}$ the influence of the grain barrier scattering gradually decreases, as the potential barrier height on the grain boundaries decreases. Above $2 \times 10^{20} \text{ cm}^{-3}$ the influence of the ionized impurity scattering increases and the effect of lattice phonons on the total mobility can be detected as well.

It can be concluded from graph 5.4.2, which shows the mobility dependence of electron

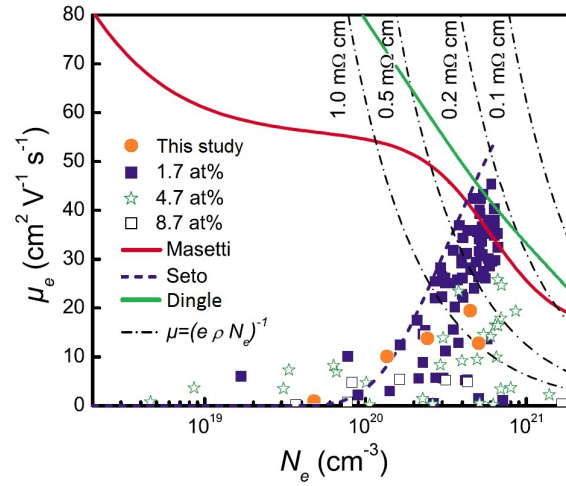


Figure 5.4.2. Electron mobility as a function of concentration (modified from [63]). Red solid curve (—) represents the semi-empirical Masetti function which describes the contribution of ionized impurity scattering and the clustering of ionized impurities. Green solid curve (—) represents analytical function which describes the ionized impurity scattering. Violet dash curve (---) represents the grain barrier scattering. Black dash-dotted curves (---) represent constant resistivity profiles. ● are samples deposited in this study, but ■, ☆ and □ are AZO films with different Al concentrations from Ref. [63].

concentration, that the grain barrier scattering is predominant in the AZO films deposited in this study. However, samples AZO2.0 and AZO2.3 with the electron concentrations of 4.6 and $4.3 \times 10^{20} \text{ cm}^{-3}$ have the mobility values of 14.4 and $18.8 \text{ cm}^2 \text{ V}^{-1} \text{ s}^{-1}$. These values are approximately two times smaller than theoretically obtainable, indicating the large concentration of trapping centers on grain boundaries [62]. An additional scattering on point defects and dislocations in the crystallites is also possible. The Al concentration of $4.1 \text{ at.}\%$ in sample AZO2.0 (Fig. 5.2.1(b)) is above the solubility limit ($2.0 - 3.0 \text{ at.}\%$) of Al in the ZnO structure without the formation of other phases [63, 64]. The high concentration of dislocations has been observed in the films with an elevated Al concentration [57]. The mobility values achieved in this study coincide with the literature data at the Al concentration of $4.7 \text{ at.}\%$ (Fig. 5.4.2). The minimum value of the mobility in Fig. 5.4.1(c) is related to the decrease of electron concentration by increasing or decreasing the $Q(\text{O}_2)$. The decrease of the electron concentration increases the potential barrier height on grain boundaries.

The resistivity of the films with the carrier concentration in the range from 1.3 to $4.6 \times 10^{20} \text{ cm}^{-3}$ is independent of temperature (Fig. 5.4.3). The thermally excited conductivity has been detected in the temperature range from 90 to 330 K for samples AZO1.5 and AZO4.5. The transition between thermally excited and metallic conductivity takes place in the electron concentration range between 4.7×10^{19} and $1.3 \times 10^{20} \text{ cm}^{-3}$. The free carrier concentration is independent of temperature for the samples with the electron concentration above $4.7 \times 10^{19} \text{ cm}^{-3}$, indicating that the AZO films are completely degenerate with donor activation energy close to zero (Fig. 5.4.4(a)). The mobility decreases with temperature in the films with higher mobility and higher carrier concentration (Fig. 5.4.4(b)). Such a behaviour is characteristic for metals. This is the strong indicator of the contribution from lattice vibrations in the total mobility. The mobility increases with temperature in samples AZO 3.0 and AZO1.5. This indicates the contribution from grain barrier scattering, as it decreases at higher temperatures.

5.5. Optical properties

The transmittance of the films on glass was measured in the range from 200 to 2500 nm (Fig. 5.5.1(a)). The transmittance of all samples is approximately 85% at 550 nm . Fig. 5.5.1(b) shows the transmittance spectra of heated ($280 \text{ }^\circ\text{C}$) AZO film during the deposition and non-heated film

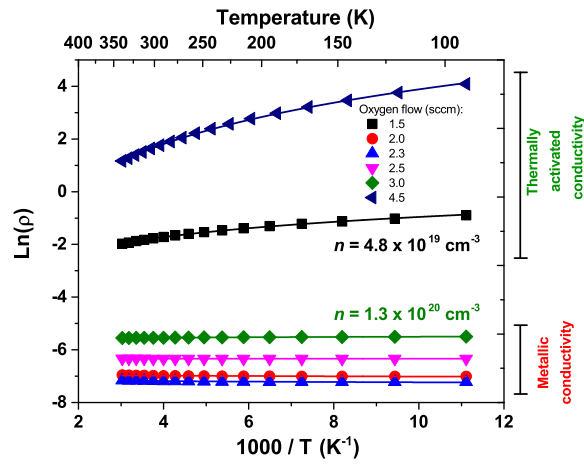


Figure 5.4.3. Resistivity of the AZO films as a function of temperature at different oxygen flows.

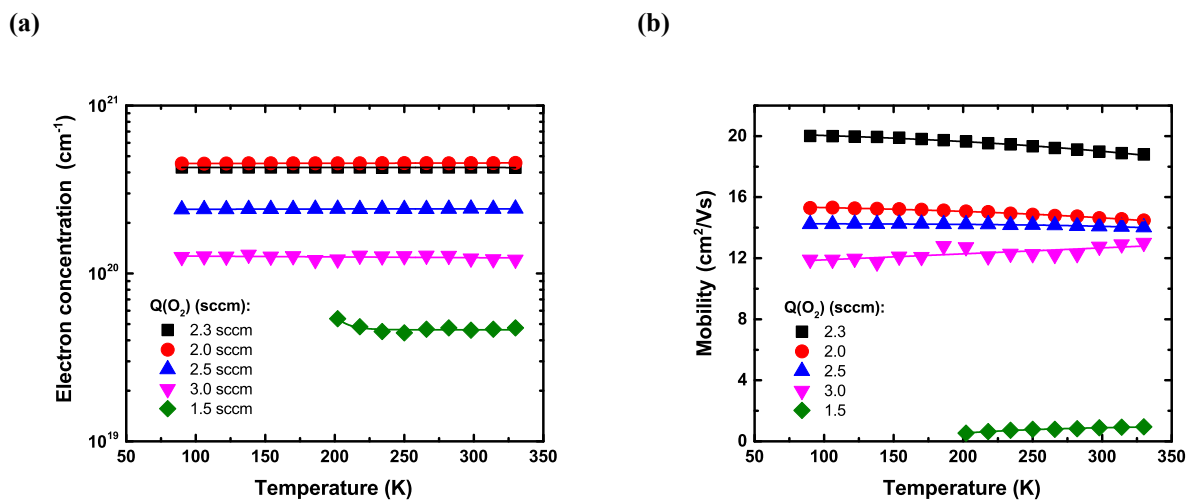


Figure 5.4.4. Free electron concentration (a) and mobility (b) as a function of temperature in the range from 90 to 330 K.

with the $Q(O_2)$ of 1.50 and 1.75 sccm, respectively. The non-heated film has significantly lower transmittance, although a higher $Q(O_2)$ was used. First, this means that the deposition process at $Q(O_2) = 1.75$ sccm and lower values is in the metallic mode. Secondly, the desorption of non-oxidized Zn atoms does not occur when the film grows on a non-heated substrate. The decrease of the transmittance in the visible light range can be explained by the formation of Zn phase in the AZO film. This fact confirms that during the substrate heating at a temperature of 280 °C, the strong desorption of non-oxidized Zn atoms from the growing film surface occurs.

The sharp absorption edge in the ultraviolet part is the fundamental absorption of ZnO (Fig. 5.5.1(a)). The shift of the absorption edge can be explained by the change of electron concentration in the conduction band. The optical band gap increases from 3.53 to 3.83 eV, when the electron concentration increases from $1,3 \times 10^{20}$ to $4,6 \times 10^{20} \text{ cm}^{-3}$, for the films deposited with the $Q(O_2)$ above 2.0 sccm (Fig. 5.5.2(a)). This is related to the Burstein-Moss effect, which is confirmed by the linear dependence between the optical band gap E_g^{opt} and $n_e^{2/3}$, as shown in Fig. 5.5.2(b).

The optical band gap shift cannot be explained by the change of electron concentration in the AZO films with elevated Al concentration, which were deposited with the $Q(O_2)$ below 2.0 sccm. The optical band gap of sample AZO1.5 has increased to 4.22 eV, while the electron concentration has decreased to $\times 10^{19} \text{ cm}^{-3}$. For sample AZO1.0 the value is even higher – 4.35 eV. The widening of the band gap could be explained by the shift of the valence and conduction bands due to the formation of a disordered ZnO structure. In this case a low temperature ZnO₂ phase [59] with the

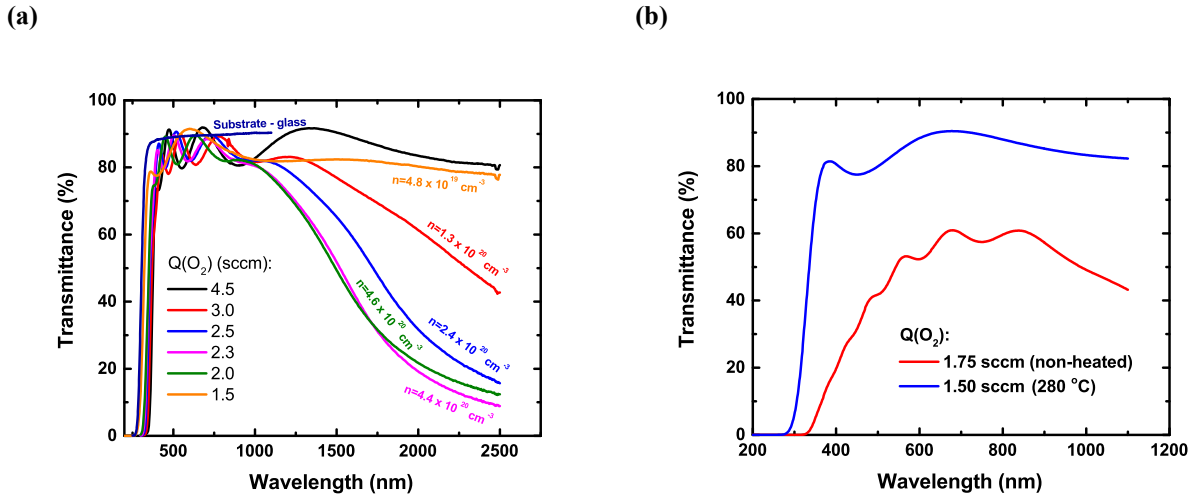


Figure 5.5.1. Transmittance of the AZO films in the range from 250 to 2500 nm (a). Substrate temperature influence on the transmittance of AZO films (b).

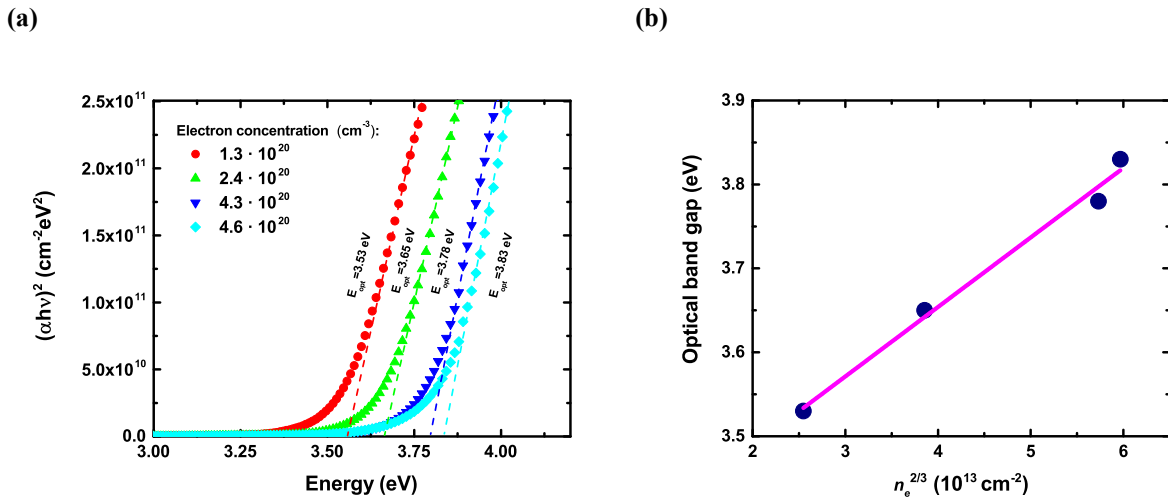


Figure 5.5.2. Optical band gap of the AZO films (a) and its dependence of electron concentration (b).

band gap value of 4.5 eV [67] could be present. At the elevated Al concentration the formation of Al_2O_3 or ZnAl_2O_4 phases is possible. Al_2O_3 and ZnAl_2O_4 have the band gap values of 7.0 – 8.8 eV [65] and 3.8 – 3.9 eV [66], respectively.

In the infrared spectra the decrease of transmittance and the increase of reflection are observed. This is due to the reflection from electron plasma oscillations. The absorption of infrared light increases with the carrier concentration. The infrared transmittance of the films deposited below 2.0 sccm $Q(O_2)$ is approximately 80 % indicating a low carrier concentration.

Electron plasma resonance frequency can be determined at a wavelength, where the light transmittance and reflection have the same value. The resonant frequency and corresponding wavelengths in the measured part of spectrum could be determined for samples AZO2.0, AZO2.3 and AZO2.5 – $9.04 \times 10^{14} \text{ Hz}$ (2085 nm), $9.29 \times 10^{14} \text{ Hz}$ (2030 nm) and $8.16 \times 10^{14} \text{ Hz}$ (2315 nm). The effective mass of electrons in the conduction band was calculated using the electron concentrations from the Hall effect measurements. The effective mass of electrons increases rapidly from $0.31m_e$ to $0.48m_e$, when the concentration of electrons rises from 2.4 to $4.6 \times 10^{20} \text{ cm}^{-3}$ (Fig. 5.5.3). This effect is explained by the non-parabolic conduction band [68].

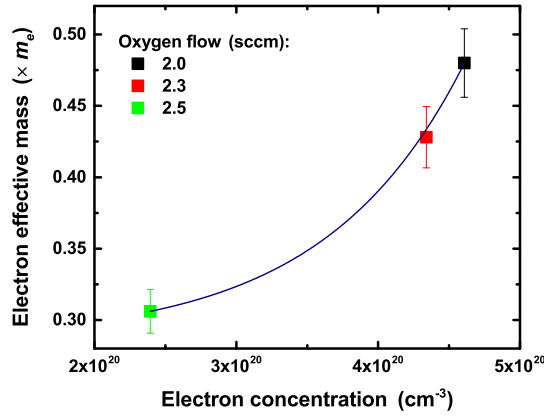


Figure 5.5.3. Electron effective mass as a function of free electron concentration in the AZO films.

5.6. Summary and conclusions

The structural, electrical and optical properties of the AZO thin films were investigated as a function of an oxygen flow in reactive DC magnetron sputtering. The oxygen flow strongly affects both the composition and structure of AZO films. Electrical and optical properties were explained by changes in the composition and structure.

The process is suitable for the deposition of highly conductive and transparent AZO thin films. The other parameters of the deposition process, such as working pressure, the temperature of a substrate, the geometrical position between a substrate and a magnetron, etc., should be optimized to improve AZO films properties.

Main conclusions:

- In the case of a low oxygen flow, the AZO films structure is X-ray amorphous because of the increased Zn/Al concentration ratio compared to the target composition (ZnAl 98:2 wt.%).
- The degree of the preferred orientation of crystallites in the *c*-axis direction increases, the lattice parameter *c* decreases and the size of the crystallites increase if the deposition process passes from a reactive to oxide mode, when the oxygen flow is increased.
- Low resistivity ($\sim 10^{-4} \Omega\text{cm}$) in *n*-type AZO films is achievable within the narrow range of oxygen flow. The electron mobility in the samples is mainly limited by the scattering on crystallographic defects (grain boundaries, point defects, dislocations) and the formation of secondary phase Al_2O_3 . The transition between thermally activated and metallic conductivity in the AZO films takes place in the electron concentration range between 4.7×10^{19} and $1.3 \times 10^{20} \text{ cm}^{-3}$.
- The transmittance of the AZO films is about 85 % in the visible light range. The optical band gap increases from 3.53 to 3.83 eV if the electron concentration in the conductive band increases from 1.3 to $4.6 \times 10^{20} \text{ cm}^{-3}$.

6. ZnO:Ir and Zn-Ir-O thin films

6.1. Deposition parameters

Two sets of samples were deposited in this study. The sets differed in both, the Ir concentration range and in the deposition parameters and geometry. The first set of samples (ZnO:Ir) was deposited with a relatively small Ir concentration, increasing it with small steps to accurately investigate the changes of the structure and properties of ZnO. The second set (Zn-Ir-O) was deposited in a wide Ir concentration range up to 66 at.%, so that the Zn/Ir concentration ratio match the ZnIr_2O_4 compound.

The ZnO:Ir thin films were deposited on glass, Si, and Ti substrates, by DC reactive magnetron co-sputtering from metallic Zn (purity 99.95 wt.%) and Ir (purity 99.6 wt.%) targets in an Ar+O₂ atmosphere (Fig. 6.1.1(a)). The samples were deposited on both non-heated and heated (300 °C) substrates. The sputtering pressure was 10 mTorr and the target to substrate distance was approximately 9 cm. The Zn target was sputtered in a constant DC mode at the power of 200W. To vary the Zn to Ir ratio in the films, the Ir target was sputtered with the power varying between 6 and 70 W. The Ar and O₂ gas flow rates were kept constant at 20 sccm and 10 sccm, respectively. In general terms, the deposition atmosphere is thought to be sufficiently oxygen rich so as not to produce oxygen deficient films with potential donor type defects, such as zinc interstitials, which promotes *n*-type conductivity.

The set of the films with a wide Ir concentration range (Zn-Ir-O) was deposited from a metallic Zn (purity 99,95 wt.%) target with Ir (purity 99,6 wt.%) pieces on the target erosion zone (Fig. 6.1.1(b)). Depending on the number of the pieces, the area ratio $S_{\text{Ir}}/S_{\text{Er.z.}}$ was varied in the range from 0.7 to 14.6 % to control an Ir concentration. The samples were deposited at the three different $Q_{(2)}/Q(\text{Ar})$ ratios – 5/20, 10/20, and 10/10. The Zn target was changed to Ir to deposit pure IrO_{2-x} .

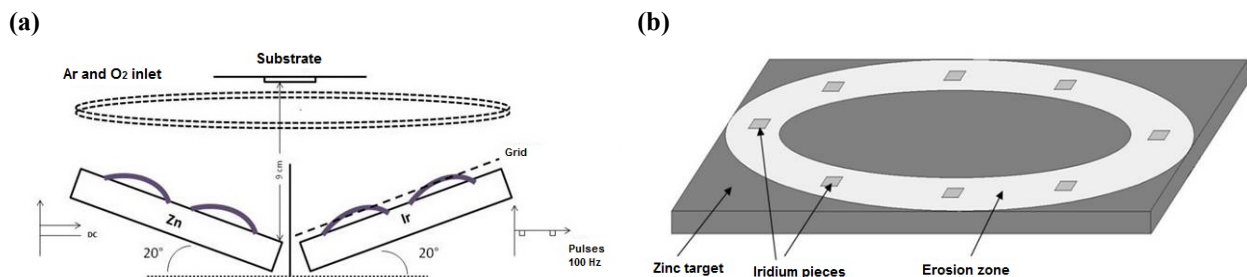


Figure 6.1.1. Two magnetron co-sputtering scheme (a). Zn target with Ir pieces on the target erosion zone (b).

6.2. Composition

The XRF spectra contained well detectable and well distinguished Zn K and Ir L fluorescence lines. The quantification of the peak intensities was made by the spectrometer built-in calculations based on the fundamental-parameter-model. The Ir concentration grows from 0.0 to 16.4 at.% if the power on the Ir target is increased from 0 to 70 W (Fig. 6.2.1(a)). The Ir concentration range of the heated samples is from 0.0 to 24.1 at.%. The difference in the Ir concentration range between the unheated and heated samples is most likely because of the slight change in the geometry of the magnetrons between the deposition of the sets.

Figure 6.2.1(b) shows that the Ir concentration in the Zn-Ir-O films is from 3 to 4 times larger compared to the amount of the Ir area on the target erosion zone ($S_{\text{Ir}}/S_{\text{Er.z.}}$). This is due to the difference in the sputtering rates between Zn and Ir and the fact that the Ir pieces were placed in the center of the erosion zone where the most intense sputtering occurs.

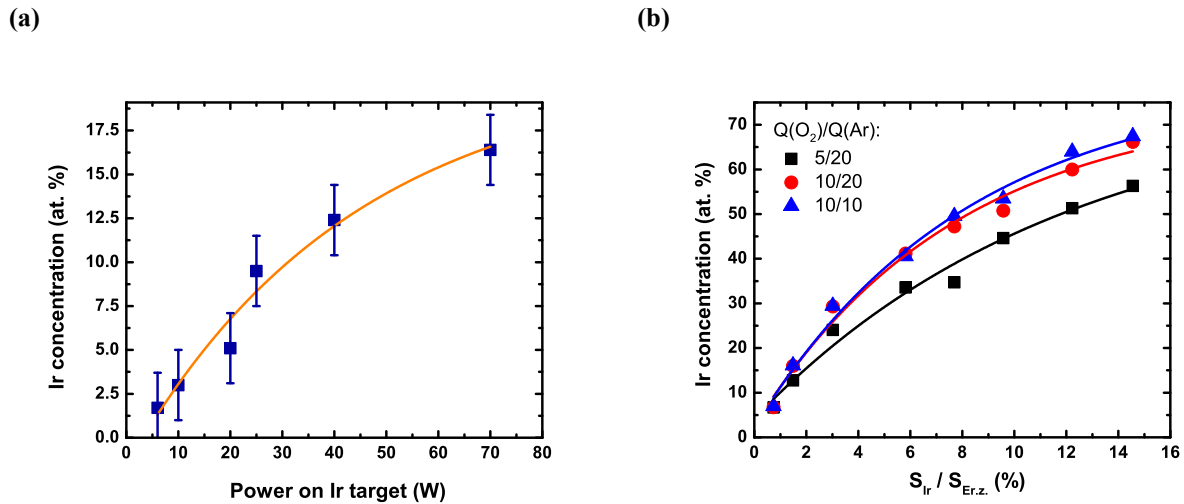


Figure 6.2.1. Ir concentration as a function of power on the Ir target (a) and the amount of Ir on the Zn target erosion zone (b).

6.3. Structure

6.3.1. X-ray diffraction measurements (XRD)

The XRD patterns of the films deposited on glass, recorded over a 2θ range of $10 - 70^\circ$, are shown in Fig. 6.3.1. A significant diffraction maximum, which corresponds to the (002) plane, was observed at around 34° for the pure and lightly doped ZnO films, indicating that the films contain a crystalline phase growing preferentially with the c -axis of the wurtzite-type ZnO (w-ZnO) lattice perpendicular to the substrate surface (Fig. 6.3.1(a)). However, the intensity of the diffraction maximum (002) is low, and comparable to the intensity of the halo peak around 23° attributed to the glass substrate, which is indicative of the presence of a significant amorphous and/or nanocrystalline phase in the films. The films lose their crystalline phase orientation with increasing iridium concentration, and an additional maximum of the (101) plane appears at 5.1 Ir at.%. Further increase of the iridium concentration degrades the crystalline structure and the films become X-ray amorphous at 12.4 Ir at.%. The XRD patterns as well as the changes in the patterns with the Ir concentration of the heated films is qualitatively the same, compared to the non-heated samples (Fig. 6.3.1(b)).

The intensity of the (002) maximum decreases with the Ir concentration. The intensity is higher for the heated samples. The crystallites in the non-heated films decreases from 7.5 to 5.0 nm if the iridium concentration is increased from 0.0 to 5.1 at.%. The average size of the crystallites in the heated films is around 9 nm in the Ir concentration range from 0.0 to 8.0 at.%. The results achieved from the Scherrer formula indicate that the ZnO:Ir films (below 5.1 Ir at.% for the non-heated and below 8.0 Ir at.% for the heated films) contain nanocrystallites with the w-ZnO structure.

The lattice parameter c in the non-heated films increases from 5.28 to 5.41 Å as the iridium concentration increases from 0.0 to 5.1 at.%. In the heated samples the lattice parameter c increases from 5,26 to 5,40 Å as the Ir concentration increases from 0.0 to 8.0 at.%. The parameter c is closer to the value of w-ZnO crystal in the case of heated samples at any given Ir concentration. It is possible to calculate the value of the lattice parameter a by using the XRD patterns of non-heated sample (5.1 Ir at.%) and heated sample (8.0 Ir at.%) with additional (101) maximum. The obtained value of the lattice parameter a is 3.30 Å for the both samples. Both parameters, a and c , are greater than the w-ZnO crystal lattice parameters $a = 3.25$ Å and $c = 5.21$ Å [35], indicating that incorporation of Ir in the structure increases the unit cell of lattice in all directions.

The results obtained from the XRD measurements indicate that the additional heating during the ZnO:Ir film growth improves the crystallization and the w-ZnO structure remains in the larger Ir concentration range. This is because by increasing the substrate temperature the adsorbed atoms on a growing film surface exhibit additional mobility, which allows to reach a thermodynamically

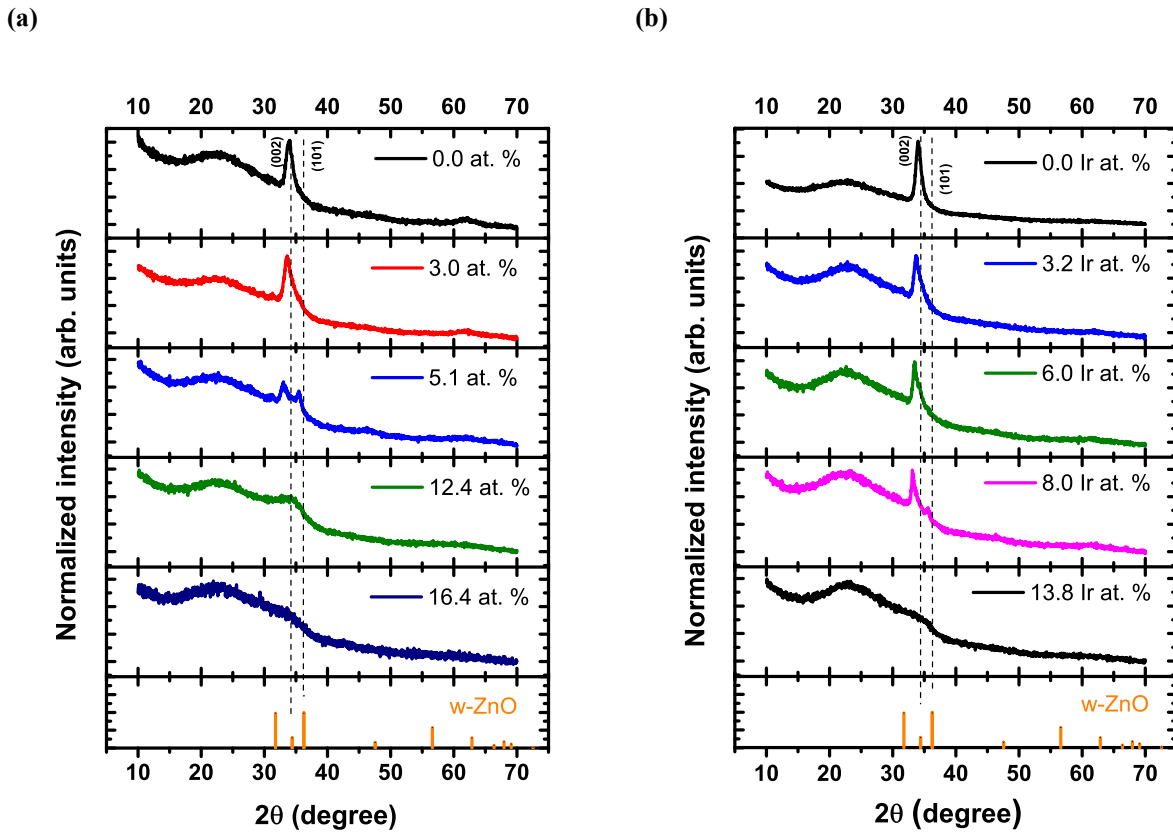


Figure 6.3.1. XRD patterns of the non-heated (a) and heated (300 °C) (b) ZnO:Ir films.

favorable position in the crystal lattice. In this case, the crystallites grows larger and the degree of crystallinity increases.

An X-ray amorphous structure remains up to 65 at.% for the both non-heated and heated samples. No phases of Zn, Ir, IrO₂ or ZnIr₂O₄ were detected. The non-heated IrO_{2-x} film is X-ray amorphous. Two maximums, that correspond to the (110) and (200) planes of the rutile (r-IrO₂) structure, are observed at 27,5° and 39,0°, respectively, in the XRD pattern of the heated IrO_{2-x} film.

The sample with the Ir concentration of 61.5 at.% was annealed to obtain a crystalline ZnIr₂O₄ structure. It is known from the literature [24] that the polycrystalline ZnIr₂O₄ film can be obtained by heating the substrate at 700 °C during pulsed laser deposition. The sample (61.5 at.%) on the glass substrate was annealed at 500 °C for 20 h, in air. The sample with the same Ir concentration on the Si substrate was annealed at 750 °C for 5 h, in air. The XRD patterns of the annealed films show IrO₂ rutile structure maximums corresponding to the planes (110), (200) and (211). The maximum at 34.8° corresponds to both the r-IrO₂ (101) plane and the w-ZnO (002) plane. The structure of the crystalline spinel ZnIr₂O₄ was not obtained after annealing.

6.3.2. X-ray absorption measurements (XAS)

The Zn K-edge XANES spectra of the Zn-Ir-O films are shown in Fig. 6.3.2(a). The XANES spectrum of the sample Zn-Ir-O (7.0 at.%) with peak positions at 9670 and 9680 eV corresponds to the polycrystalline w-ZnO spectrum and indicates four coordinated Zn (ZnO₄ tetrahedrons) [69]. As the concentration increases, the peak at 9670 eV gets wider with additional contribution from the lower energies, but the peak at 9680 eV disappears. This indicates an increase of disorder around Zn ions and changes in the geometry of ZnO₄ tetrahedra. However, Zn retains the coordination of 4 across the entire Ir concentration range.

The Ir L₃-edge XANES spectra of the Zn-Ir-O films are shown in Fig. 6.3.2(b). As the Ir concentration increases, the absorption peak moves towards the lower energy. Such a behavior indicates a decrease in the valence of Ir [70]. Referring to work [71], it can be concluded that the

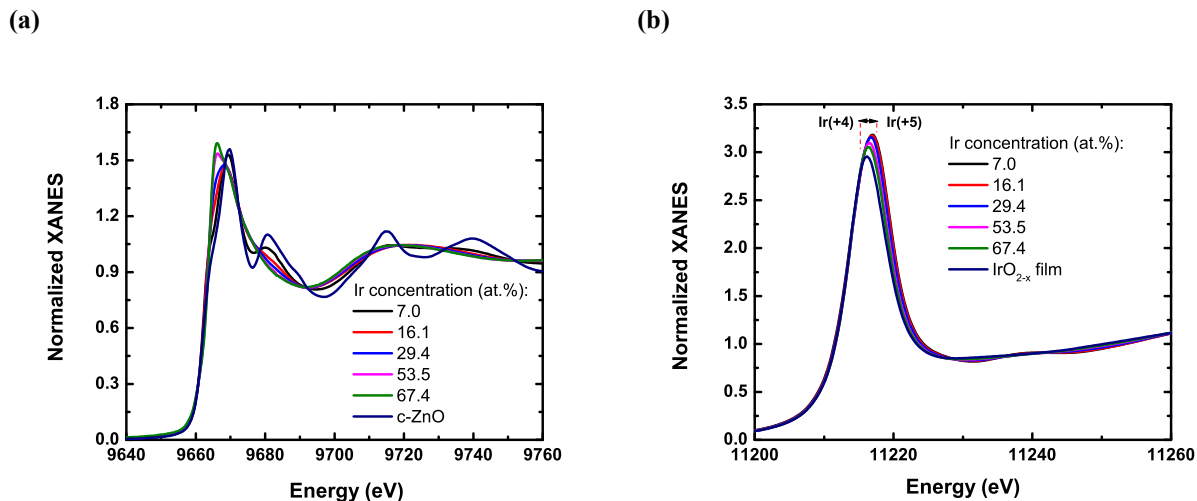


Figure 6.3.2. Zn K-edge (a) un Ir L₃-edge (b) XANES spectra of the Zn-Ir-O thin films with different Ir at.% concentration and reference compounds – polycrystalline bulk w-ZnO and amorphous IrO_{2-x} film.

Ir ion charge state changes from +5 to +4 when the Ir concentration increases from 30 to 50 at.%.

The Fourier transforms of the experimental Zn K-edge and Ir L₃-edge extended X-ray absorption fine structure spectra (FT-EXAFS-Zn,Ir) of the ZnO:Ir films and reference compounds are shown in Fig. 6.3.3. The features in the FT-EXAFS correspond to the superposition of the various atom distribution functions for Zn and Ir. But one should take into account that the amplitude and distances are distorted by photoelectron back scattering amplitudes and phase shifts [72].

The first feature of FT-EXAFS-Zn (Fig. 6.3.3(a)) at about 1.5 Å originates from the first coordination shell of Zn – nearest oxygens [73]. The second feature, at about 3.0 Å, comes mainly from the second coordination shell, here Zn-Zn (with real distance 3.2 and 3.25 Å [73]). The feature at about 4.3 Å originates from further Zn-Zn pairs (4.57 Å [73]). The FT-EXAFS-Zn spectra of the Zn-Ir-O thin films are different from the polycrystalline (c-ZnO) reference spectrum. However, there are some similarities between ZnO:Ir (7.0 Ir at.%) and the c-ZnO reference up to the third coordination shell around Zn. The FT-EXAFS-Zn feature for the first coordination shell is qualitatively the same, only an amplitude damping with an increase of Ir

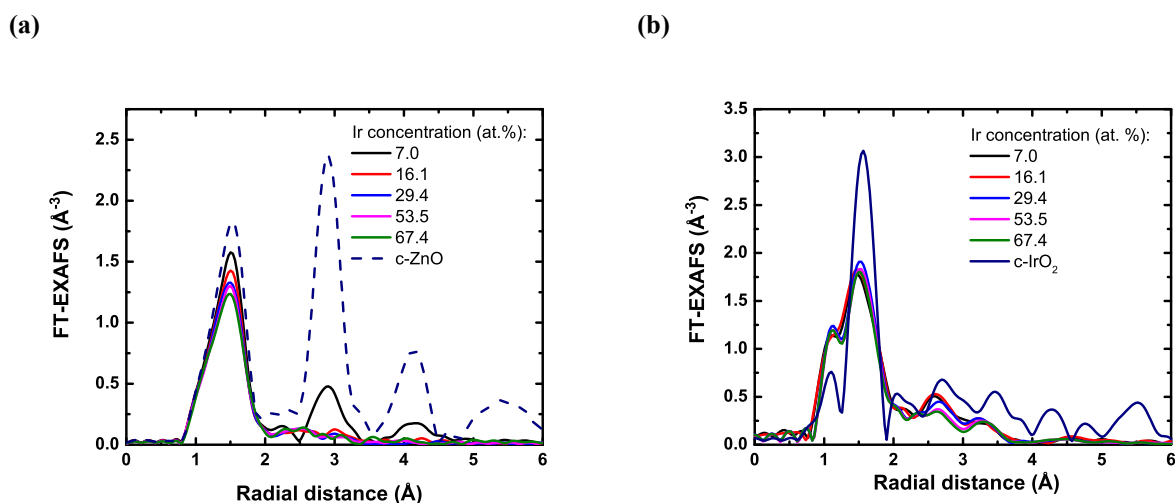


Figure 6.3.3. Modulus of the FT-EXAFS spectra at Zn K-edge (a) and Ir L₃-edge (b) for the Zn-Ir-O thin films and reference compounds – polycrystalline bulk c-ZnO and c-IrO₂.

concentration happens, caused by increasing disorder in the Zn-O distances. Other features up to 4.5 Å seen in c-ZnO are also present, but with significantly lower amplitudes, indicating increasing disorder. All the features above 4.5 Å in the FT-EXAFS-Zn signal of the ZnO:Ir (7.0 Ir at.%) are missing, due to significant structural disorder. In the FT-EXAFS-Zn spectrum of the ZnO:Ir (16.4 Ir at.%), even the feature around 2.9 Å, which corresponds to the second coordination shell, vanishes, indicating that the ZnO structure becomes completely amorphous for higher Ir concentrations.

Also in the FT-EXAFS-Ir spectra (Fig. 6.3.3(b)), all the features above 4.5 Å are missing. However, features above 2.3 Å correspond to the mix of the multiple scattering signal from the first coordination shell (Ir-O-O triangles) with some signal from the second coordination shell Ir-*Me* (where *Me* can be Zn or Ir). This is different from the Zn, where we cannot see any significant signal from the second coordination shell for higher Ir concentrations.

Therefore, from the EXAFS measurements, we can conclude that for small Ir concentrations (up to 7.0 Ir at.%), the ZnO structure is nanocrystalline, but for higher Ir concentrations (e.g. 16.4 Ir at.%), the structure becomes completely amorphous.

6.3.3. Surface morphology

The granular surface morphology with the grain size up to 25 nm is observed for the pure ZnO_x films (Fig. 6.3.4(a)).

The surface morphology of the non-heated samples changes rapidly in the Ir concentration range from 5.1 to 9.5 at.%. It correlates with the transition from the nanocrystalline structure to the amorphous state. The surface morphology of the sample ZnO:Ir (9,5 Ir at.%) is no longer granular (Fig. 6.3.4(c)) but contains nanosized (150 – 250 nm) pores visible in the cross-section image (Fig. 6.3.4(f)). The pore size decreases and does not exceed 100 nm when the Ir concentration is increased up to 24.1 at.% (Fig. 6.3.4(d)). The pores are completely disappeared, and a smooth surface is formed for the sample with the Ir concentration of 40.6 at.%.

The granular surface morphology remains up to 8.0 at.% for the heated samples, but there is the change of a grain shape. The grains have more pronounced edges when the Ir concentration is increased.

6.3.4. Vibrational properties (FTIR and Raman measurements)

FTIR measurements. The samples were irradiated perpendicularly to the films surface and under the angle of 45° with non-polarised IR light. Only the transverse optical mode E₁^{TO} around 410 cm⁻¹ is observed (Fig. 6.3.5(a)) if the samples are irradiated perpendicularly. It is because the dipole moment of the E₁^{TO} mode is perpendicular to the *c*-axis and the crystallites are oriented in the direction of *c*-axis. An additional A₁^{LO} mode is detected at 575 cm⁻¹ when the samples are irradiated under the angle of 45° (Fig. 6.3.5(b)). In this geometry there is the component of electromagnetic field that is parallel to the *c*-axis and interact with LO vibrations having a wave vector perpendicular to the films surface. Qualitatively similar spectra were obtained for the heated samples.

The integrated intensity of the E₁^{TO} band decreases for both the non-heated and heated samples with the Ir concentration, but it is higher for the heated samples. The frequency of the E₁^{TO} mode of the films with a relatively low Ir concentration (< 5.1 at.%) coincides within the error range with the w-ZnO crystal value of 410 cm⁻¹. Above 5.1 Ir at.%, the frequency rapidly increases and reaches the value of 475 cm⁻¹ at 16.4 Ir at.%. For the heated films the rapid change of the frequency occurs only above 20.0 Ir at.%. The FWHM of the band increases for the non-heated and heated films with the Ir concentration. For the heated films the FWHM is lower compared to the non-heated films at any given Ir concentration.

The results of the FTIR measurements indicate that the degree of w-ZnO structure crystallinity is higher and remains in the wider Ir concentration range in the case of heated ZnO:Ir films. These results correlate with the XRD measurements. By increasing the Ir concentration, the nano-crystallites becoming smaller and the structural atomic network gradually becoming different from the crystalline w-ZnO until a wurtzite phase becomes undetectable at 12.4 Ir at.%

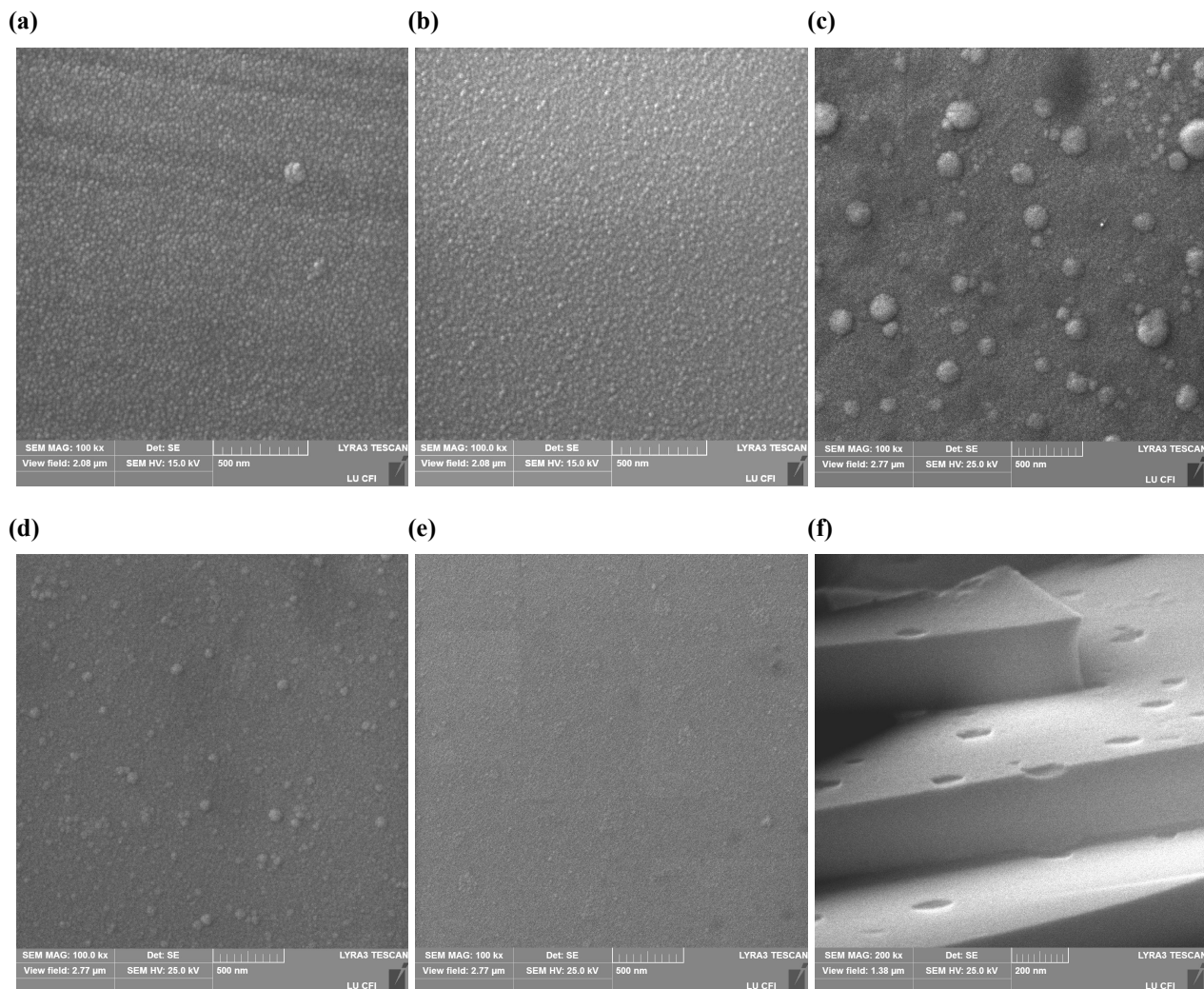


Figure 6.3.4. Surface morphology of the non-heated ZnO:Ir films (0.0 (a), 5.1 (b), 9.5 (c), 24.1 (d) and 40.6 (e) Ir at.%). Cross-section image of the sample 9.5 Ir at.% (f).

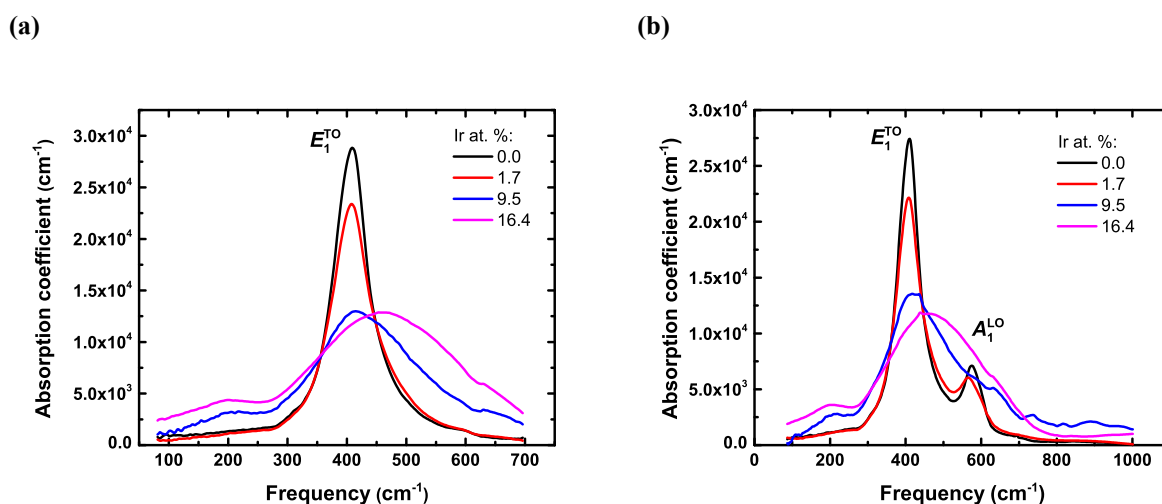


Figure 6.3.5. IR absorption spectra of the non-heated ZnO:Ir films, when they are irradiated perpendicularly (a) or under the angle of 45° (b).

for the non-heated samples and at 24.1 Ir at.% for the heated samples.

Raman measurements. The Raman spectra of the ZnO:Ir films are shown in Fig. 6.3.6(a) and 6.3.6(b). In the Raman spectrum of the pure ZnO_x film, only A_1^{LO} , E_2^{high} and E_2^{low} bands (573, 437

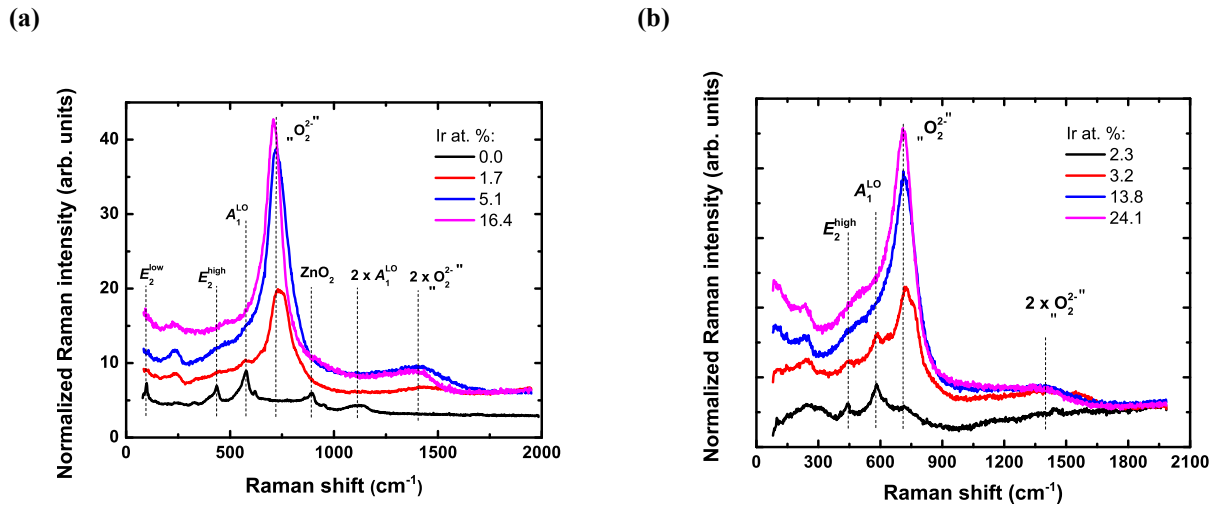


Figure 6.3.6. Raman spectra of the non-heated (a) and heated (b) ZnO:Ir films. Vertical dash lines together with designations indicate the characteristic w-ZnO and additional observed Raman bands.

and 97 cm^{-1} , respectively) were detected due to the experimental configuration and film orientation ($z(x+y, x+y)\bar{z}$). The band around 860 cm^{-1} originates from the ZnO_2 phase [74]. At high $Q(\text{O}_2)$ a ZnO_2 phase formation is possible which is a low temperature phase in the Zn-O system [59]. The wide band around 1100 cm^{-1} originates from the second order mode $2A_1^{\text{LO}}$.

The Raman intensity for the pure ZnO_x films is relatively low compared to the new vibration mode around 720 cm^{-1} which appears after Ir incorporation. However, signs of the A_1^{LO} and E_2^{high} bands are still observable up to 3.0 Ir at.% for the non-heated films and up to 3.2 Ir at.% for the heated films. There is no clear evidence about the origin of the intense 720 cm^{-1} band. However, the present results do not support the assumption that the band arises from the IrO_2 phase [75]. If the IrO_2 phase were present, there should be an even more intense E_g band around 560 cm^{-1} [76, 77]. Theoretically, the E_g band is forbidden in the backscattering configuration if the crystallites are oriented in the [001] direction [78], which is unlikely in this case due to the disordered structure. We performed Raman measurements under oblique angle to check whether oriented IrO_2 crystallites are responsible for the 720 cm^{-1} band, but the obtained spectra did not exhibit any changes. The band around 1400 cm^{-1} is the second order mode of the 720 cm^{-1} band and behaves the same way when the Ir concentration is increased.

The integrated intensity of the intense 720 cm^{-1} band increases up to 5.1 at.% at first and starts to decrease above 9.5 Ir at.%. This is one more piece of evidence that the band does not originate from the IrO_2 phase, because in that case, and also taking into account that the Raman intensity is directly proportional to the concentration of the active species, the intensity should have increased with the Ir concentration. The frequency shifts close to exponentially from 735 to 710 cm^{-1} as the Ir concentration grows from 1.7 to 16.4 at.%. The FWHM undergoes a rapid step-like decrease from 120 to 85 cm^{-1} in the Ir concentration range from 5.1 to 9.5 at.%. The behaviour of the frequency and the FWHM indicates that the change of the structure taking place upon an increase of Ir concentration up to 9.5 at.% causes the relaxation of the vibration mode.

It can be suggested that the 720 cm^{-1} band which is not IR active is caused by the presence of peroxide ions, and the band may be attributed to the stretching mode of the O_2^{2-} (Fig. 6.3.7(a)). Although the frequency of vibrations of the O_2 molecule is approximately twice the frequency of 720 cm^{-1} , the frequency of ionised O_2 molecules with increased O–O bond lengths is reduced (Fig. 6.3.7(b)). Since the pure ZnO spectrum does not exhibit a 720 cm^{-1} band, the presence of Ir causes structural changes favourable for the generation of O_2^{2-} with the O–O distance appropriate for the 720 cm^{-1} stretching frequency. Crystalline ZnO_2 with an O–O bond length of approximately 1.5 \AA [79] has the characteristic Raman band around 840 cm^{-1} [74], while the theoretical studies on ZnO_2 molecules show that the O_2^{2-} stretching frequency can be as low as 682 cm^{-1} with an O–O

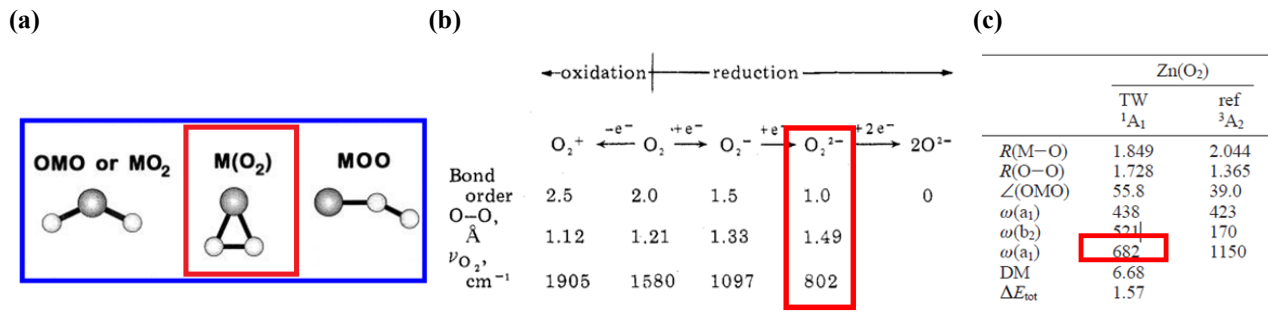


Figure 6.3.7. Three different structures of dioxide isomers (a) [80]. Bond length and frequency depending on the charge of O₂ molecule (b) [81]. Equilibrium bond length (R, Å), bond angle (∠ (OMO), °), harmonic vibrational frequency (ω, cm⁻¹) un dipole moment (DM, D) of Zn(O₂) molecule (c) [80].

bond length of 1.7 Å [80] (Fig. 6.3.7(c)). For the stretching frequency of 720 cm⁻¹, the appropriate O—O distance should be between 1.5 and 1.7 Å.

The framework of the O₂²⁻ in the nanoporous oxide C12A7 (12CaO · 7Al₂O₃) with the frequency around 770 cm⁻¹ is deeply studied in Ref. [82, 83]. A high partial pressure of oxygen favours the formation of the O₂²⁻, which is accomplished by a diffusion of O₂ molecules from the atmosphere into nanocages of C12A7, where they react with O²⁻ radicals. Following this approach, the molecular oxygen used in the deposition process of the ZnO:Ir films could be caged in the nanopores and produce the peroxide ions O₂²⁻. SEM images (Fig. 6.3.4) reveal that ZnO:Ir and Zn-Ir-O films have a porous surface morphology.

Fig. 6.3.8(a) shows the Raman spectra of the non-heated Zn-Ir-O films in a wide Ir concentration range. The 720 cm⁻¹ band begins to overlap with a wide band formed at lower frequencies at 26.0 Ir at.%. At 41.8 Ir at.% the 720 cm⁻¹ band is completely blurred and a wide band has been formed in the range from 300 to 700 cm⁻¹. This spectrum remains unchanged up to the pure a-IrO_{2-x} film and no additional vibration bands were detected in the Ir concentration range from 41.8 to 100.0 at.%.

The 720 cm⁻¹ band is well detectable up to 36.9 Ir at.% for the heated films (Fig. 6.3.8(b)). A wide vibration band at around 545 cm⁻¹, which corresponds to the vibration mode E_g of the r-IrO₂ phase, is observed in the Raman spectrum for the Zn-Ir-O film with 61.5 Ir at.%. It can be concluded that the heated Zn-Ir-O films with the Ir concentration above 61.5 at.% contain IrO₂

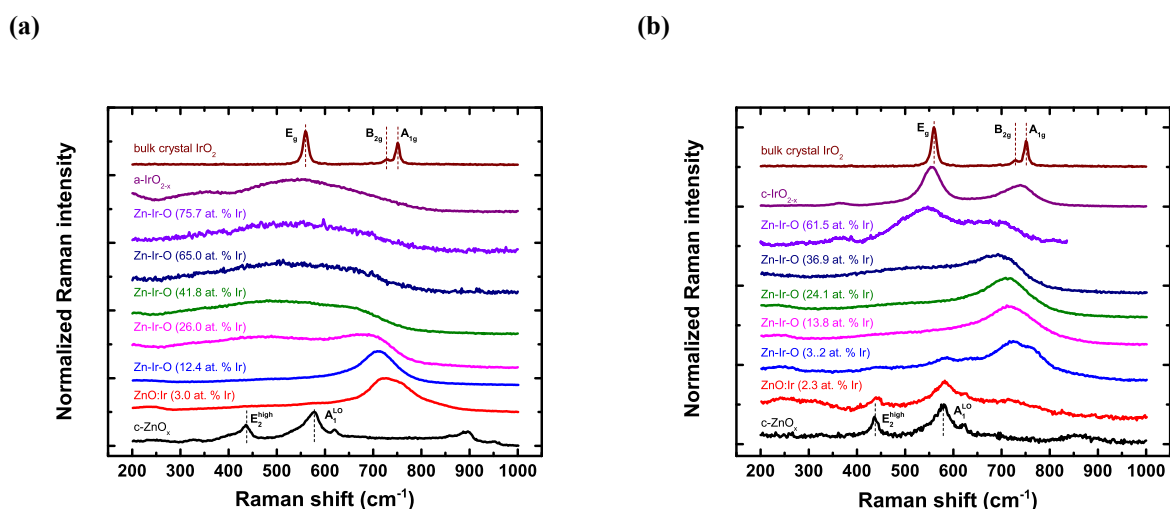


Figure 6.3.8. Raman spectra of the non-heated (a) and heated (b) Zn-Ir-O films. Vertical dash lines together with designations indicate the characteristic w-ZnO and r-IrO₂ Raman bands.

nanocrystallites. The E_g vibration mode and the overlapped B_{2g} and A_{1g} modes are observed for the pure IrO_{2-x} film. The vibration bands are wider compared to the polycrystalline IrO_2 reference indicating the lower degree of crystallinity.

6.4. Electrical properties

The electrical properties of the ZnO:Ir and Zn-Ir-O films were studied by measuring the DC electrical conductivity at 300 K and as a function of temperature between 90 K and 330 K.

The resistivity of the films with low iridium atomic concentration (0.0 – 9.5 at.%) is extremely high and exceeds the measurable range ($> 10^7 \Omega\text{cm}$). The high oxygen content used in the sputtering ambient was obviously sufficient to prevent the formation of zinc interstitials, which are native donors in the ZnO and the origin of spontaneous n -type conductivity [84]. However, the iridium impurities at low concentrations do not appear to have generated sufficient levels of defects to increase the conductivity significantly. A measurable resistivity of $8.3 \times 10^1 \Omega\text{cm}$ appears at 12.4 at.% of iridium, which correlates with the w -ZnO structure disappearing completely according to the structural and vibrational investigation. For the ZnO:Ir films deposited at 573 K, a measurable resistivity of $1.2 \times 10^{-1} \Omega\text{cm}$ appears at 19.1 Ir at.%, which again correlates with the fact that in this case the w -ZnO structure becomes undetectable for Ir concentrations above 20.0 at.%. The resistivity of the non-heated films decreases exponentially from 8.3×10^1 to $2.6 \times 10^{-4} \Omega\text{cm}$ if the Ir concentration is increased from 12.4 to 100.0 at.% (Fig. 6.4.1(a)).

It was not possible to measure the Hall effect in the Zn-Ir-O films. A stable additional voltage difference between the contacts was not detected by placing the samples in the magnetic field, although the maximum current value of 20 mA was used to increase the Hall voltage. Only in the heated pure IrO_{2-x} film the Hall voltage was detected. Results showed p -type conductivity with the resistivity of $2.5 \times 10^{-4} \Omega\text{cm}$ at 300 K. In this sample the hole concentration and Hall mobility values were $4.8 \times 10^{22} \text{cm}^{-3}$ and $0.51 \text{cm}^2\text{V}^{-1}\text{s}^{-1}$, respectively. The low mobility value indicates that in the case of the Zn-Ir-O films most likely the mobility is too low to measure the Hall voltage accurately.

The temperature dependant resistivity and an Arrhenius plot of $\ln(\rho)$ vs. $1000/T$ (K^{-1}) is shown in Fig. 6.4.1(b). The resistivity decreases with the temperature which is typical for semiconductors in the Ir concentration range from 12.4 to 47.2 at.%. A linear function was used to approximate data to calculate the carrier activation energy (E_A) from a slope value. The E_A value decreases exponentially from 141 to 0,12 meV if the Ir concentration is increased from 12.4 to 100.0 at.%. However, it can be seen in Fig. 6.4.1(b) that the function $\ln\rho(1000/T)$ is not

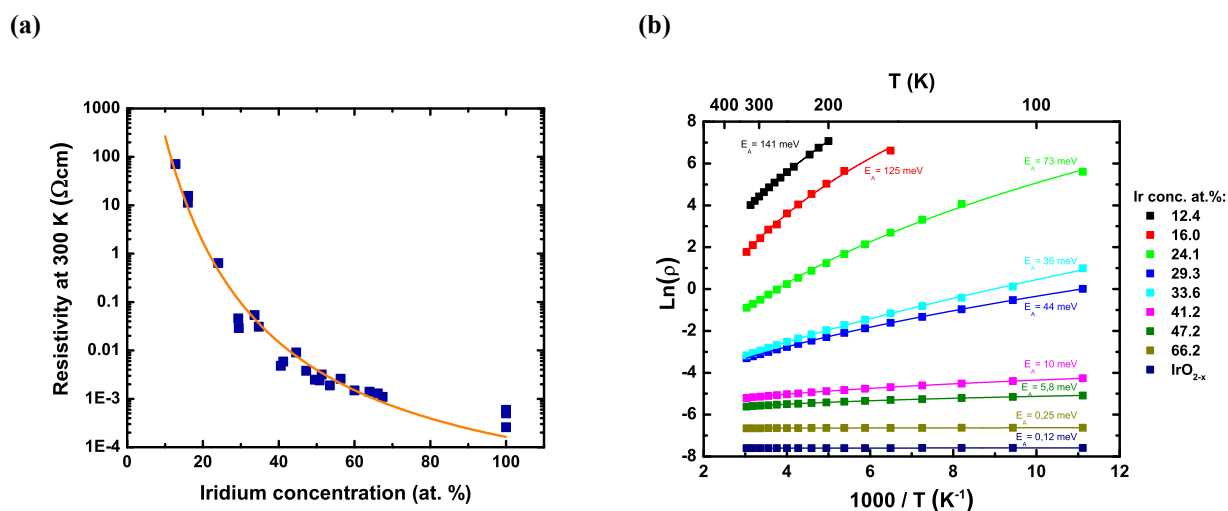


Figure 6.4.1. Resistivity of the Zn-Ir-O films at room temperature as a function of Ir concentration (a). Arrhenius plot $\ln(\rho)$ vs. $1000/T$ (K^{-1}) for the films with different Ir concentration (data are approximated with the function $\ln(\rho) = a + bT^\xi$) (b).

completely linear in the Ir concentration range from 12.4 to 47.2 at.%.

Mott's variable range hopping conductivity mechanism [85] could be the case in the semiconductors with a strongly disorder structure and the mechanism is widely used in the literature to interpret experimental data. The movement of charge carriers in electric field in the hopping conductivity is realized as tunnelling transitions with the absorption or emission of phonons within the narrow strip of the localized states in the vicinity of the Fermi level. The temperature dependant resistivity in the hopping model is described by formula:

$$\rho = \rho_0 \exp\left(-\frac{T_0}{T}\right)^\xi, \quad (6.1)$$

where T_0 is a constant, but exponent ξ could have the value of 0.25 (without Coulomb interaction between electrons [85]) or 0.5 (with Coulomb interaction between electrons [86]). If the ξ value after the approximation of data is close to 1, then the conductivity mechanism is thermally activated like in non-degenerate semiconductors. If the ξ value is close to 0, then the conductivity is temperature independent like in fully degenerate semiconductors.

The experimental data were approximated by the function $\ln(\rho) = a + bT^\xi$, where a , b and ξ are fitting parameters, to determine the conduction model (Fig. 6.4.1(b)). The ξ value is in the range from 0.12 to 0.63 with the average value of 0.33, if the Ir concentration is in the range from 12.4 to 44.6 at.% (Fig. 6.4.2). The average value indicates the Mott's variable range hopping conductivity in the films. The resistivity above 47.2 Ir at.% is almost temperature independent.

The dependence of the Seebeck voltage on temperature was measured by varying temperature difference from -5 to $+5$ K. The average temperature was kept constant at 308 K. The Seebeck coefficient was calculated as a slope coefficient of the obtained relations (Fig. 6.4.3(a)). The sign of the Seebeck coefficient changes from negative to positive (from -13.1 to $+6.8$ $\mu\text{V}/\text{K}$) if the iridium concentration increases from 12.4 to 16.4 at.% (Fig. 6.4.3(b)).

There is no clear interpretation of what causes the transition from n -type to p -type conductivity. However, it can be concluded that at lower Ir concentration both electron and holes participate in the total conductivity. The change of the conductivity type indicates several competing conductivity mechanisms. In the Ir concentration range from 16.4 to 44.6 the holes could travel by hopping through the amorphous ZnO matrix with Zn vacancies [87, 88] or through the complexes containing Ir. The holes move freely above 47.2 Ir at.% like in degenerate semiconductor with metallic conductivity. IrO_2 films are known as a p -type conductor [89]. The results of electrical measurements indicate that conductivity and the position of Fermi level changes with the Ir concentration.

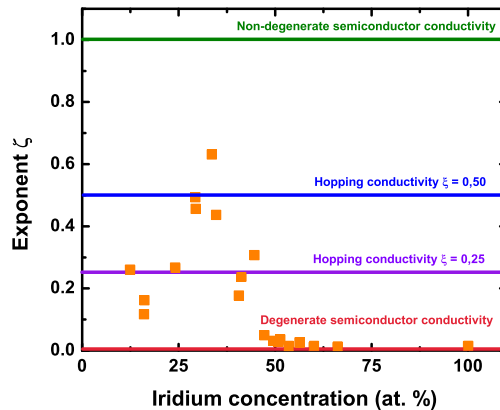


Figure 6.4.2. Conductivity mechanism depending on Ir concentration.

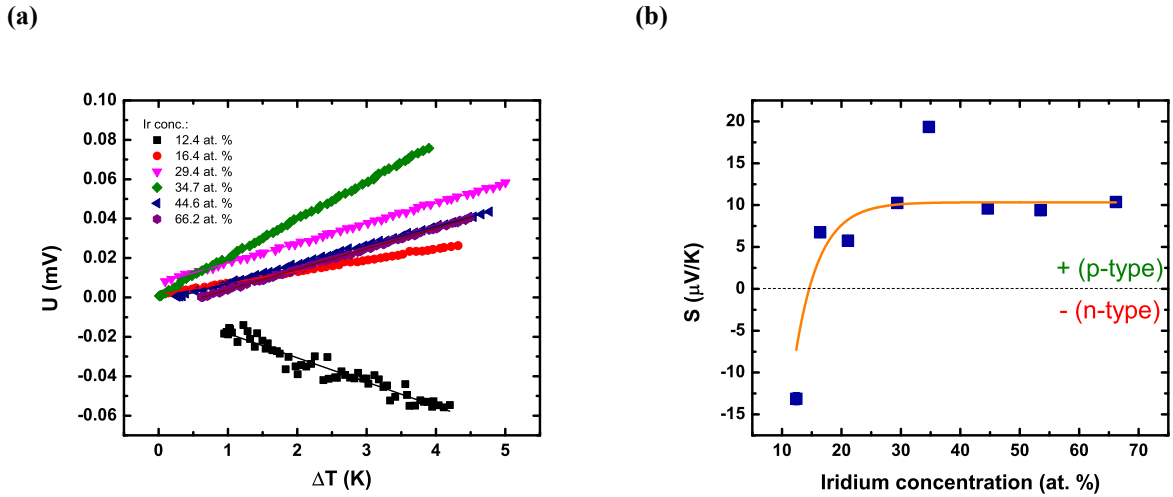


Figure 6.4.3. Thermoelectric measurements (a) and the Seebeck coefficient (b) of the Zn-Ir-O films with different Ir concentrations.

6.5. Optical properties

The transmittance decreases sharply throughout the measured spectrum for both the non-heated and heated films when the Ir concentration is increased (Fig. 6.5.1). The absorption coefficient at 550 nm (2.25 eV) increases linearly from 5.1×10^2 to $2.5 \times 10^4 \text{ cm}^{-1}$, if the Ir concentration is increased from 0.0 to 100.0 at.% (Fig. 6.5.2(a)). This indicates, that the Ir containing phase is directly responsible of the decrease of transmittance. In the case of Ir (+4) oxide (IrO_2) absorption below 2.5 eV increases due to Ir $d-d$ optical transitions and free electron absorption, but above 3.0 eV due to O p -Ir d transitions [90].

The optical band gap of the non-heated ZnO:Ir thin films does not shift with the iridium concentration up to 5.1 Ir at.% and remains around 3.3 eV, which is the value of w-ZnO films (Fig. 6.5.2(b)). Above 5.1 Ir at.% the sharp absorption edge can not be observed. The absorption edge dependence of the Ir concentration of the heated films is qualitatively the same compared to the non-heated films. It is worth mentioning that there is no blue shift of the optical band gap together with the ZnO amorphization, as was reported in Ref. [91, 92]. Furthermore, the ZnO_2 phase detected in the pure ZnO_x Raman spectrum should be at low concentration, because ZnO_2 exhibits a larger band gap than w-ZnO [67].

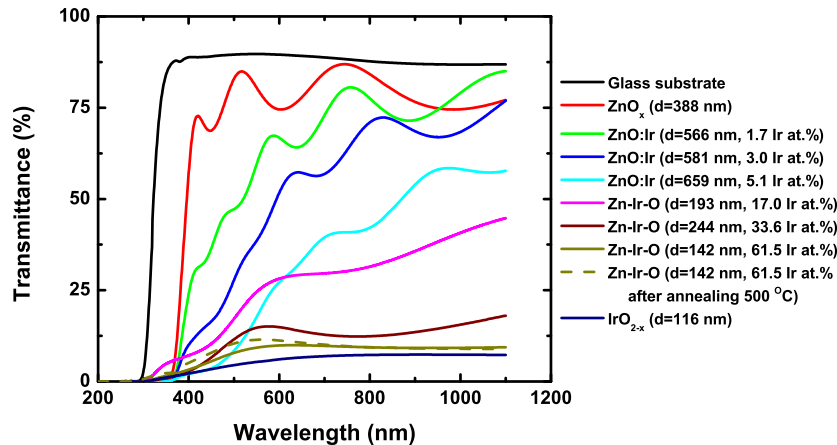


Figure 6.5.1. Transmittance of the non-heated ZnO_x , ZnO:Ir, Zn-Ir-O and IrO_{2-x} films in the range from 200 to 1100 nm.

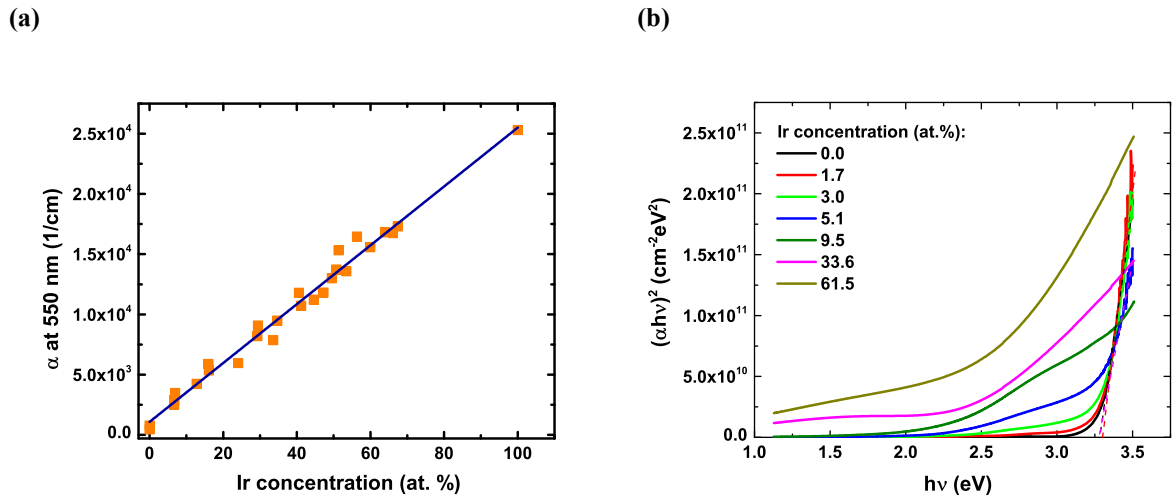


Figure 6.5.2. Absorption coefficient at 550 nm as a function of Ir concentration (a). Tauc plot $(\alpha h\nu)^2$ vs. $h\nu$ to determine the optical band gap of the non-heated ZnO:Ir and Zn-Ir-O films (b).

6.6. Summary and conclusions

Reactive magnetron co-sputtering deposition from two targets is shown to be a suitable technique to dope thin films very accurately by using the sputtering power as the composition control parameter.

The structure, electrical and optical properties of the ZnO:Ir and Zn-Ir-O thin films as a function of Ir concentration were studied. The degree of crystallinity is decreased and the conductivity and visible light absorption is increased with the ZnO_x doping with Ir.

The findings of the study are principally new, because this compound is little studied. The studies of *p*-type TCO thin films based on ZnO have a tremendous practical significance.

Main conclusions:

- The structure of the nano-crystalline ZnO_x film gradually becomes amorphous by adding and increasing the Ir concentration. The nano-crystalline structure remains in the wider Ir concentration range if the substrate during the deposition is heated up to a temperature of 300 °C. Zn mainly is located in ZnO₄ tetrahedra, but Ir in IrO₆ octahedra in the amorphous Zn-Ir-O structure.
- After the Ir incorporation, the ZnO structure could contain peroxide O₂²⁻ ions that are responsible for the intense Raman band around 720 cm⁻¹.
- The valence state of Ir ions in the Zn-Ir-O films changes from +5 to +4 by increasing the Ir concentration from 30.0 to 50.0 at.%.
- The conductivity of the Zn-Ir-O films increases sharply with the Ir concentration together with the total disappearance of w-ZnO structure. The conduction type undergoes the transition from *n*-type to *p*-type in the Ir concentration range between 12.4 and 16.4 at.%. The electrical mechanism changes from the thermally activated hopping to metallic-like conductivity at about 50 Ir at.%.
- The absorption coefficient increases linearly in the visible light range with the Ir concentration.

Main thesis

1. An Al to Zn concentration ratio sharply increases and the structure of AZO films changes from a crystalline wurtzite structure to an X-ray amorphous structure, if the reactive magnetron sputtering process changes from a reactive to metallic mode by decreasing the oxygen flow and the substrate temperature is above 250 °C. It is explained by the non-oxidized Zn desorption from a growing film surface.
2. Nano-crystalline ZnO thin films deposited by magnetron sputtering in a reactive Ar and O₂ atmosphere gradually become amorphous by adding and increasing the Ir content in the films. Ir impurities obstruct the growth of crystalline ZnO structure. The transition from the nano-crystalline to amorphous phase occurs in the Ir concentration range from 7 to 16 at.%, if the substrate is not heated intentionally during the deposition (< 50 °C). The structure of heated samples at a temperature of 300 °C during the deposition process becomes completely amorphous in the Ir concentration range from 20 to 24 at.%. The amorphous structure remains up to 100 Ir at.%.
3. The structural atomic network of non-heated amorphous Zn-Ir-O (7 – 30 Ir at.%) thin films mainly consists of ZnO₄ tetrahedra. After Ir incorporation, the intense Raman band at approximately 720 cm⁻¹ appears and is attributed to the vibrations of peroxide O₂²⁻ ions.
4. The electrical conductivity of ZnO:Ir thin films sharply increases when the structure of the films changes from nano-crystalline to amorphous. The resistivity of the films decreases exponentially from 83 Ωcm to 2.6 × 10⁻⁴ Ωcm when the Ir concentration is increased from 12.4 to 100 at.%. This is explained by the formation of an iridium-containing conducting phase. The type of the conductivity changes from *n*- to *p*-type in the Ir concentration range from 12.4 to 16.4 at.%.

Bibliography

- [1] H. Hosono, D. C. Paine, Handbook of transparent conductors, Springer Science & Business Media, 2010.
- [2] T. Minami, Transparent conducting oxide semiconductors for transparent electrodes, *Semiconductor Science and Technology* 20 (4) (2005) S35.
- [3] M. Bender, W. Seelig, C. Daube, H. Frankenberger, B. Ocker, J. Stollenwerk, Dependence of film composition and thicknesses on optical and electrical properties of ITO–metal–ITO multilayers, *Thin Solid Films* 326 (1) (1998) 67–71.
- [4] C. Guillén, J. Herrero, TCO/metal/TCO structures for energy and flexible electronics, *Thin Solid Films* 520 (1) (2011) 1–17.
- [5] G. Torrisi, I. Crupi, S. Mirabella, A. Terrasi, Robustness and electrical reliability of AZO/Ag/AZO thin film after bending stress, *Solar Energy Materials and Solar Cells* 165 (2017) 88–93.
- [6] L. Hu, H. Wu, Y. Cui, Metal nanogrids, nanowires, and nanofibers for transparent electrodes, *MRS bulletin* 36 (10) (2011) 760–765.
- [7] M.-G. Kang, L. J. Guo, Nanoimprinted semitransparent metal electrodes and their application in organic light-emitting diodes, *Advanced Materials* 19 (10) (2007) 1391–1396.
- [8] J. Van Deelen, L. Klerk, M. Barink, H. Rendering, P. Voorthuijzen, A. Hovestad, Improvement of transparent conducting materials by metallic grids on transparent conductive oxides, *Thin Solid Films* 555 (2014) 159–162.
- [9] S. De, T. M. Higgins, P. E. Lyons, E. M. Doherty, P. N. Nirmalraj, W. J. Blau, J. J. Boland, J. N. Coleman, Silver nanowire networks as flexible, transparent, conducting films: extremely high DC to optical conductivity ratios, *ACS nano* 3 (7) (2009) 1767–1774.
- [10] Y.-H. Duan, Y. Duan, P. Chen, Y. Tao, Y.-Q. Yang, Y. Zhao, High-performance flexible Ag nanowire electrode with low-temperature atomic-layer-deposition fabrication of conductive-bridging ZnO film, *Nanoscale research letters* 10 (1) (2015) 90.
- [11] E. M. Doherty, S. De, P. E. Lyons, A. Shmeliov, P. N. Nirmalraj, V. Scardaci, J. Joimel, W. J. Blau, J. J. Boland, J. N. Coleman, The spatial uniformity and electromechanical stability of transparent, conductive films of single walled nanotubes, *Carbon* 47 (10) (2009) 2466–2473.
- [12] V. H. Souza, E. Flahaut, A. J. Zarbin, Conducting, transparent and flexible substrates obtained from interfacial thin films of double-walled carbon nanotubes, *Journal of Colloid and Interface Science* 502 (2017) 146–152.
- [13] S. Bae, H. Kim, Y. Lee, X. Xu, J.-S. Park, Y. Zheng, J. Balakrishnan, T. Lei, H. R. Kim, Y. I. Song, et al., Roll-to-roll production of 30-inch graphene films for transparent electrodes, *Nature nanotechnology* 5 (8) (2010) 574–578.
- [14] W. A. de Heer, Epitaxial graphene: A new electronic material for the 21st century, *Mrs Bulletin* 36 (8) (2011) 632–639.
- [15] F. Bonaccorso, Z. Sun, T. Hasan, A. Ferrari, Graphene photonics and optoelectronics, *Nature photonics* 4 (9) (2010) 611–622.
- [16] Y. Sun, Q. Wu, G. Shi, Graphene based new energy materials, *Energy & Environmental Science* 4 (4) (2011) 1113–1132.
- [17] Y. H. Kim, C. Sachse, M. L. Machala, C. May, L. Müller-Meskamp, K. Leo, Highly conductive PEDOT: PSS electrode with optimized solvent and thermal post-treatment for ITO-free organic solar cells, *Advanced Functional Materials* 21 (6) (2011) 1076–1081.
- [18] B. Szyszka, W. Dewald, S. K. Gurram, A. Pflug, C. Schulz, M. Siemers, V. Sittinger, S. Ulrich, Recent developments in the field of transparent conductive oxide films for spectral selective coatings, electronics and photovoltaics, *Current Applied Physics* 12 (2012) S2–S11.
- [19] A. Janotti, C. G. Van de Walle, Fundamentals of zinc oxide as a semiconductor, *Reports on progress in physics* 72 (12) (2009) 126501.

- [20] K. Ellmer, A. Bikowski, Intrinsic and extrinsic doping of ZnO and ZnO alloys, *Journal of Physics D: Applied Physics* 49 (41) (2016) 413002.
- [21] S. Fujita, Wide-bandgap semiconductor materials: For their full bloom, *Japanese Journal of Applied Physics* 54 (3) (2015) 030101.
- [22] M. Dekkers, G. Rijnders, D. H. Blank, ZnIr_2O_4 , a p-type transparent oxide semiconductor in the class of spinel zinc- d^6 -transition metal oxide, *Appl. Phys. Lett.* 90 (2) (2007) 21903–21903.
- [23] S. Narushima, H. Mizoguchi, K.-i. Shimizu, K. Ueda, H. Ohta, M. Hirano, T. Kamiya, H. Hosono, A p-Type Amorphous Oxide Semiconductor and Room Temperature Fabrication of Amorphous Oxide p–n Heterojunction Diodes, *Advanced Materials* 15 (17) (2003) 1409–1413.
- [24] J. M. Dekkers, Transparent conducting oxides on polymeric substrates by pulsed laser deposition, University of Twente, 2007.
- [25] K. Ellmer, Past achievements and future challenges in the development of optically transparent electrodes, *Nature Photonics* 6 (12) (2012) 809–817.
- [26] K. H. Zhang, K. Xi, M. G. Blamire, R. G. Egdell, P-type transparent conducting oxides, *Journal of Physics: Condensed Matter* 28 (38) (2016) 383002.
- [27] S. C. Dixon, D. O. Scanlon, C. J. Carmalt, I. P. Parkin, n-Type doped transparent conducting binary oxides: an overview, *Journal of Materials Chemistry C* 4 (29) (2016) 6946–6961.
- [28] M. Chen, Z. Pei, X. Wang, Y. Yu, X. Liu, C. Sun, L. Wen, Intrinsic limit of electrical properties of transparent conductive oxide films, *Journal of Physics D: Applied Physics* 33 (20) (2000) 2538.
- [29] P. Drude, Zur elektronentheorie der metalle, *Annalen der Physik* 306 (3) (1900) 566–613.
- [30] H. Ohta, H. Hosono, Transparent oxide optoelectronics, *Materials Today* 7 (6) (2004) 42–51.
- [31] A. Banerjee, K. Chattopadhyay, Recent developments in the emerging field of crystalline p-type transparent conducting oxide thin films, *Progress in Crystal Growth and Characterization of Materials* 50 (1) (2005) 52–105.
- [32] H. Kawazoe, H. Yanagi, K. Ueda, H. Hosono, Transparent *p*-type conducting oxides: design and fabrication of *p-n* heterojunctions, *Mrs Bulletin* 25 (8) (2000) 28–36.
- [33] G. Hautier, A. Miglio, G. Ceder, G.-M. Rignanese, X. Gonze, Identification and design principles of low hole effective mass *p*-type transparent conducting oxides, *Nature communications* 4 (2013) 2292.
- [34] E. Fortunato, P. Barquinha, R. Martins, Oxide semiconductor thin-film transistors: a review of recent advances, *Advanced materials* 24 (22) (2012) 2945–2986.
- [35] Ü. Özgür, Y. I. Alivov, C. Liu, A. Teke, M. Reshchikov, S. Doğan, V. Avrutin, S.-J. Cho, H. Morkoc, A comprehensive review of ZnO materials and devices, *J. Appl. Phys.* 98 (4) (2005) 041301.
- [36] J. R. Chelikowsky, An oxygen pseudopotential: Application to the electronic structure of ZnO, *Solid State Communications* 22 (6) (1977) 351–354.
- [37] H. Mizoguchi, M. Hirano, S. Fujitsu, T. Takeuchi, K. Ueda, H. Hosono, ZnRh_2O_4 : A p-type semiconducting oxide with a valence band composed of a low spin state of Rh^{3+} in a $4d^6$ configuration, *Appl. Phys. Lett.* 80 (7) (2002) 1207–1209.
- [38] S. Samanta, Study of systematic trends in electronic and optical properties within ZnM_2O_4 (M = Co, Rh, Ir) family by FPLAPW method with PBE and TB-mBJ potentials, *Optical Materials* 45 (2015) 141–147.
- [39] D. O. Scanlon, G. W. Watson, Band gap anomalies of the $\text{ZnM}_2^{\text{III}}\text{O}_4$ (M^{III} = Co, Rh, Ir) spinels, *Phys. Chem. Chem. Phys.* 13 (20) (2011) 9667–9675.
- [40] D. M. Ramo, P. D. Bristowe, The effect of defects and disorder on the electronic properties of ZnIr_2O_4 , *J. Chem. Phys.* 141 (8) (2014) 084704.
- [41] H. Jarrett, A. W. Sleight, H. H. Kung, J. Gillson, Photoelectrochemical and solid-state properties of LuRhO_3 , *Journal of Applied Physics* 51 (7) (1980) 3916–3925.

- [42] M. Amini, H. Dixit, R. Saniz, D. Lamoen, B. Partoens, The origin of p-type conductivity in ZnM_2O_4 (M = Co, Rh, Ir) spinels, *Phys. Chem. Chem. Phys.* 16 (6) (2014) 2588–2596.
- [43] K. Ellmer, Magnetron sputtering of transparent conductive zinc oxide: relation between the sputtering parameters and the electronic properties, *Journal of Physics D: Applied Physics* 33 (4) (2000) R17.
- [44] Crystallography Open Database, <http://www.crystallography.net/> (2016).
- [45] V. Briois, E. Fonda, S. Belin, L. Barthe, C. La Fontaine, F. Langlois, M. Ribbens, F. Villain, Samba: The 4–40 keV x-ray absorption spectroscopy beamline at soleil, in: *UVX 2010-10e Colloque sur les Sources Cohérentes et Incohérentes UV, VUV et X; Applications et Développements Récents*, EDP Sciences, 2011, pp. 41–47.
- [46] R. Wendt, K. Ellmer, Desorption of Zn from a growing ZnO: Al-film deposited by magnetron sputtering, *Surface and Coatings Technology* 93 (1) (1997) 27–31.
- [47] R. Hong, H. Qi, J. Huang, H. He, Z. Fan, J. Shao, Influence of oxygen partial pressure on the structure and photoluminescence of direct current reactive magnetron sputtering ZnO thin films, *Thin Solid Films* 473 (1) (2005) 58–62.
- [48] M. Yuste, R. E. Galindo, I. Caretti, R. Torres, O. Sánchez, Influence of the oxygen partial pressure and post-deposition annealing on the structure and optical properties of ZnO films grown by dc magnetron sputtering at room temperature, *Journal of Physics D: Applied Physics* 45 (2) (2011) 025303.
- [49] Y.-N. Xu, W. Ching, Electronic, optical, and structural properties of some wurtzite crystals, *Physical Review B* 48 (7) (1993) 4335.
- [50] S. Youssef, P. Combette, J. Podlecki, R. A. Asmar, A. Foucaran, Structural and optical characterization of ZnO thin films deposited by reactive RF magnetron sputtering, *Crystal Growth and Design* 9 (2) (2008) 1088–1094.
- [51] C.-H. Chao, P.-W. Chi, D.-H. Wei, Investigations on the Crystallographic Orientation Induced Surface Morphology Evolution of ZnO Thin Films and Their Wettability and Conductivity, *The Journal of Physical Chemistry C* 120 (15) (2016) 8210–8219.
- [52] N. Fujimura, T. Nishihara, S. Goto, J. Xu, T. Ito, Control of preferred orientation for ZnOx films: control of self-texture, *Journal of Crystal Growth* 130 (1-2) (1993) 269–279.
- [53] M. Brett, R. Parsons, Structural properties of non-stoichiometric zinc oxide films, *Journal of Materials Science* 22 (10) (1987) 3611–3614.
- [54] K. Ellmer, T. Welzel, Reactive magnetron sputtering of transparent conductive oxide thin films: Role of energetic particle (ion) bombardment, *Journal of Materials Research* 27 (5) (2012) 765–779.
- [55] J. Cuomo, R. Gambino, J. Harper, J. Kuptsis, Origin and effects of negative ions in the sputtering of intermetallic compounds, *IBM Journal of Research and Development* 21 (6) (1977) 580–583.
- [56] P. Pokorný, J. Bulíř, J. Lančok, J. Musil, M. Novotný, Generation of positive and negative oxygen ions in magnetron discharge during reactive sputtering of alumina, *Plasma Processes and Polymers* 7 (11) (2010) 910–914.
- [57] S. Yoshioka, F. Oba, R. Huang, I. Tanaka, T. Mizoguchi, T. Yamamoto, Atomic structures of supersaturated Zn O–Al₂O₃ solid solutions, *Journal of Applied Physics* 103 (1) (2008) 014309.
- [58] K. Ellmer, F. Kudella, R. Mientus, R. Schieck, S. Fiechter, Influence of discharge parameters on the layer properties of reactive magnetron sputtered ZnO: Al films, *Thin Solid Films* 247 (1) (1994) 15–23.
- [59] K. Ellmer, Resistivity of polycrystalline zinc oxide films: current status and physical limit, *Journal of Physics D: Applied Physics* 34 (21) (2001) 3097.
- [60] K. Knutsen, A. Galeckas, A. Zubiaga, F. Tuomisto, G. Farlow, B. Svensson, A. Y. Kuznetsov, Zinc vacancy and oxygen interstitial in ZnO revealed by sequential annealing and electron irradiation, *Physical Review B* 86 (12) (2012) 121203.

- [61] K. Ellmer, R. Mientus, Carrier transport in polycrystalline transparent conductive oxides: A comparative study of zinc oxide and indium oxide, *Thin solid films* 516 (14) (2008) 4620–4627.
- [62] F. M. Hossain, J. Nishii, S. Takagi, A. Ohtomo, T. Fukumura, H. Fujioka, H. Ohno, H. Koinuma, M. Kawasaki, Modeling and simulation of polycrystalline ZnO thin-film transistors, *Journal of Applied Physics* 94 (12) (2003) 7768–7777.
- [63] S. Cornelius, M. Vinnichenko, N. Shevchenko, A. Rogozin, A. Kolitsch, W. Möller, Achieving high free electron mobility in ZnO: Al thin films grown by reactive pulsed magnetron sputtering, *Applied Physics Letters* 94 (4) (2009) 042103.
- [64] S. Cornelius, M. Vinnichenko, Al in ZnO—From doping to alloying: An investigation of Al electrical activation in relation to structure and charge transport limits, *Thin Solid Films* 605 (2016) 20–29.
- [65] E. O. Filatova, A. S. Konashuk, Interpretation of the changing the band gap of Al₂O₃ depending on its crystalline form: connection with different local symmetries, *The Journal of Physical Chemistry C* 119 (35) (2015) 20755–20761.
- [66] H. Dixit, N. Tandon, S. Cottenier, R. Saniz, D. Lamoen, B. Partoens, V. Van Speybroeck, M. Waroquier, Electronic structure and band gap of zinc spinel oxides beyond LDA: ZnAl₂O₄, ZnGa₂O₄ and ZnIn₂O₄, *New Journal of Physics* 13 (6) (2011) 063002.
- [67] W. Chen, Y. Lu, M. Wang, L. Kroner, H. Paul, H.-J. Fecht, J. Bednarcik, K. Stahl, Z. Zhang, U. Wiedwald, et al., Synthesis, thermal stability and properties of ZnO nanoparticles, *The Journal of Physical Chemistry C* 113 (4) (2009) 1320–1324.
- [68] C. A. Niedermeier, S. Rhode, K. Ide, H. Hiramatsu, H. Hosono, T. Kamiya, M. A. Moram, Electron effective mass and mobility limits in degenerate perovskite stannate BaSnO₃, *Physical Review B* 95 (16) (2017) 161202.
- [69] A. Kuzmin, S. Larcheri, F. Rocca, Zn K-edge XANES in nanocrystalline ZnO, in: *Journal of Physics: Conference Series*, Vol. 93, IOP Publishing, 2007, p. 012045.
- [70] A. Cruz, L. Abad, N. Carretero, J. Moral-Vico, J. Fraxedas, P. Lozano, G. Subías, V. Padial, M. Carballo, J. Collazos-Castro, et al., Iridium oxohydroxide, a significant member in the family of iridium oxides. Stoichiometry, characterization, and implications in bioelectrodes, *The Journal of Physical Chemistry C* 116 (8) (2012) 5155–5168.
- [71] J.-H. Choy, D.-K. Kim, S.-H. Hwang, G. Demazeau, D.-Y. Jung, XANES and EXAFS Studies on the Ir-O Bond Covalency in Ionic Iridium Perovskites, *J. Am. Chem. Soc.* 117 (33) (1995) 8557–8566.
- [72] V. Aksenov, M. Koval'chuk, A. Y. Kuz'min, Y. Purans, S. Tyutyunnikov, Development of methods of EXAFS spectroscopy on synchrotron radiation beams: Review, *Crystallography Reports* 51 (6) (2006) 908–935.
- [73] J. Timoshenko, A. Anspoks, A. Kalinko, A. Kuzmin, Local structure and dynamics of wurtzite-type ZnO from simulation-based EXAFS analysis, *physica status solidi (c)* 11 (9–10) (2014) 1472–1475.
- [74] H. Bai, X. Liu, Green hydrothermal synthesis and photoluminescence property of ZnO 2 nanoparticles, *Materials Letters* 64 (3) (2010) 341–343.
- [75] G. Michail, V. Kambylafka, I. Kortidis, K. Tsagaraki, M. Androulidaki, G. Kiriakidis, V. Binas, M. Modreanu, E. Aperathitis, On the growth of transparent conductive oxide ternary alloys Zn–Ir–O (ZIRO) by the means of rf magnetron co-sputtering, *Thin Solid Films*.
- [76] A. V. Korotcov, Y.-S. Huang, K.-K. Tiong, D.-S. Tsai, Raman scattering characterization of well-aligned RuO₂ and IrO₂ nanocrystals, *Journal of Raman spectroscopy* 38 (6) (2007) 737–749.
- [77] P. Liao, C. Chen, W. Ho, Y. Huang, K. Tiong, Characterization of IrO₂ thin films by Raman spectroscopy, *Thin Solid Films* 301 (1) (1997) 7–11.
- [78] R.-S. Chen, A. Korotcov, Y.-S. Huang, D.-S. Tsai, One-dimensional conductive IrO₂ nanocrystals, *Nanotechnology* 17 (9) (2006) R67.

- [79] R. Thapa, S. Ghosh, S. Sinthika, E. M. Kumar, N. Park, Magnetic, elastic and optical properties of zinc peroxide (ZnO 2): First principles study, *Journal of Alloys and Compounds* 620 (2015) 156–163.
- [80] G. Gutsev, B. Rao, P. Jena, Systematic study of oxo, peroxy, and superoxy isomers of 3d-metal dioxides and their anions, *The Journal of Physical Chemistry A* 104 (51) (2000) 11961–11971.
- [81] L. Vaska, Dioxygen-metal complexes: toward a unified view, *Accounts of Chemical Research* 9 (5) (1976) 175–183.
- [82] S. Yang, J. N. Kondo, K. Hayashi, M. Hirano, K. Domen, H. Hosono, Formation and Desorption of Oxygen Species in Nanoporous Crystal $12\text{CaO} \cdot 7\text{Al}_2\text{O}_3$, *Chemistry of materials* 16 (1) (2004) 104–110.
- [83] K. Kajihara, S. Matsuishi, K. Hayashi, M. Hirano, H. Hosono, Vibrational Dynamics and Oxygen Diffusion in a Nanoporous Oxide Ion Conductor $12\text{CaO} \cdot 7\text{Al}_2\text{O}_3$ Studied by ^{18}O Labeling and Micro-Raman Spectroscopy, *The Journal of Physical Chemistry C* 111 (40) (2007) 14855–14861.
- [84] J. C. Fan, K. Sreekanth, Z. Xie, S. Chang, K. V. Rao, p-Type ZnO materials: theory, growth, properties and devices, *Progress in Materials Science* 58 (6) (2013) 874–985.
- [85] N. Mott, Conduction in glasses containing transition metal ions, *Journal of Non-Crystalline Solids* 1 (1) (1968) 1–17.
- [86] A. Efros, B. Shklovskii, Coulomb gap and low temperature conductivity of disordered systems, *Journal of Physics C: Solid State Physics* 8 (4) (1975) L49.
- [87] L. Pan, S. Wang, W. Mi, J. Song, J.-J. Zou, L. Wang, X. Zhang, Undoped ZnO abundant with metal vacancies, *Nano Energy* 9 (2014) 71–79.
- [88] A. Renaud, L. Cario, X. Rocquelfelte, P. Deniard, E. Gautron, E. Faulques, T. Das, F. Cheviré, F. Tessier, S. Jobic, Unravelling the origin of the giant Zn deficiency in wurtzite type ZnO nanoparticles, *Scientific reports* 5.
- [89] P. Patil, P. Chigare, S. Sadale, T. Seth, D. Amalnerkar, R. Kawar, Thickness-dependent properties of sprayed iridium oxide thin films, *Materials chemistry and physics* 80 (3) (2003) 667–675.
- [90] A. K. Goel, G. Skorinko, F. H. Pollak, Optical properties of single-crystal rutile RuO_2 and IrO_2 in the range 0.5 to 9.5 eV, *Physical Review B* 24 (12) (1981) 7342.
- [91] S. Tan, B. Chen, X. Sun, W. Fan, H. S. Kwok, X. Zhang, S. Chua, Blueshift of optical band gap in ZnO thin films grown by metal-organic chemical-vapor deposition, *Journal of Applied Physics* 98 (1) (2005) 13505–13505.
- [92] J. Bruncko, A. Vincze, M. Netrvalova, P. Šutta, D. Hasko, M. Michalka, Annealing and recrystallization of amorphous ZnO thin films deposited under cryogenic conditions by pulsed laser deposition, *Thin Solid Films* 520 (2) (2011) 866–870.

Author's publication list

1. M. Zubkins, R. Kalendarev, J. Gabrusenoks, A. Plaude, A. Zitolo, A. Anspoks, K. Pudzs, K. Vilnis, A. Azens and J. Purans, Changes in structure and conduction type upon addition of Ir to ZnO thin films, *Thin Solid Films* 636 (2017) 694-701.
2. M. Zubkins, R. Kalendarev, J. Gabrusenoks, K. Smits, K. Kundzins, K. Vilnis, A. Azens, J. Purans, Raman, electron microscopy and electrical transport studies of x-ray amorphous Zn-Ir-O thin films deposited by reactive DC magnetron sputtering, *IOP Conf. Ser.: Mater. Sci. Eng.* 77 (2015) 012035:1-5.
3. M. Zubkins, R. Kalendarev, J. Gabrusenoks, K. Vilnis, A. Azens, J. Purans, Structural, electrical and optical properties of zinc-iridium oxide thin films deposited by DC reactive magnetron sputtering, *Phys. Status Solidi (c)* 11 (2014) 1493-1496.
4. M. Zubkins, R. Kalendarev, K. Vilnis, A. Azens, J. Purans, Structural, electrical and optical characteristics of Al-doped zinc oxide thin films deposited by reactive magnetron sputtering, *IOP Conf. Ser.: Mater. Sci. Eng.* 49 (2013) 012057 (4pp).

Participation in conferences

International conferences (oral presentations):

1. FMNT–2015, Vilnius, Lithuania, 05.10.2015–08.10.2015, *Structural, optical and electrical properties of ZnO:Ir thin films deposited by reactive magnetron co-sputtering*;
2. E–MRS Fall Meeting 2015, Warsaw, Poland, 15.09.2015–18.09.2015, *Structural, electrical and optical properties of ZnO:Ir thin films deposited by reactive magnetron co-sputtering*;
3. 5th International Conference on HIPIMS, Sheffield, United Kingdom, 02.07.2014–03.07.2014, *Structural, electrical and optical properties of Zn-Ir-O thin films*;
4. Developments in Optics and Communications 2014, Riga, Latvia, 09.04.2014–12.04.2014, *Structural, electrical and optical properties of Zn-Ir-O thin films*;
5. E–MRS Fall Meeting 2013, Warsaw, Poland, 16.09.2013–20.09.2013, *Structural, electrical and optical properties of zinc-iridium oxide thin films deposited by reactive magnetron sputtering*.

International conferences (poster presentations):

1. FMNT–2017, Tartu, Estonia, 24.04.2017–27.04.2017, *Structure, vibration properties and p-type conductivity of the Zn-Ir-O thin films deposited by reactive dc magnetron sputtering*;
2. EuroNanoForum 2015, Riga, Latvia, 10.06.2015–12.06.2015, *Structural and optical properties of ZnO:Ir thin films deposited by reactive magnetron co-sputtering*;
3. Reactive Sputter Deposition 2014, Gent, Belgium, 11.12.2014–12.12.2014, *Amorphous Zn-Ir-O thin films deposited by DC reactive magnetron sputtering*;
4. FMNT–2014, Riga, Latvia, 29.09.2014–02.10.2014, *Raman, electron microscopy and electrical transport studies of x-ray amorphous Zn-Ir-O thin films deposited by reactive DC magnetron sputtering*.

ISSP UL annual conferences: 3 oral and 4 poster presentations.

Participation in schools

1. IFF Spring School 2016, Germany, Jülich;
2. Advanced materials and technologies 2015, Lithuania, Palanga;
3. Baltic Neutron School 2014, Estonia, Tartu.

Acknowledgements

I would like to express my greatest gratitude to my supervisor Dr. **Jurim Purans** about the possibility to develop the doctoral thesis at the EXAFS Spectroscopy Laboratory. Thank You for the long-term contribution to my scientific development, from the development of the Bachelor thesis to the doctoral dissertation. I have great pleasure working in Your laboratory. Thank You for your trust and support.

Also, I would like to thank Dr. **Roberts Kalendarevs** for his contribution to my scientific growth when working together with vacuum equipment. Thanks to Robert for valuable discussions and work on thin films deposition.

Thanks you Dr. **Jevgenijs Gabrusenoks** on Raman and FTIR spectroscopy measurements, their interpretation, valuable discussions and patience explaining the results. Thanks to Dr. **Andris Azens** for sharing his experience about thin films science, valuable discussions and reviewing my scientific papers. Thank you **Kaspars Vilnis** for the technical preparation of vacuum equipment. Thank you Mg. **Andrejs Kursits** for the spelling correction of the doctoral thesis. Also, thanks to the rest of EXAFS spectroscopy lab. staff – Dr. **Andris Anspoks**, Dr. **Alekseis Kuzmins**, Dr. **Vera Skvorcova**, Dr. **Nina Mironova-Ulmane** and Dr. **Leonids Chugunovs**.

Thank you Dr. **Linards Skuja** for teaching the X-ray fluorescence spectroscopy basics. Thank you Mg. **Aina Plaude** and Mg. **Reinis Ignatans** for X-ray diffraction measurements and interpretation. Thank you Dr. **Georgijs Chikvaidze** for FTIR spectroscopy measurements. Thank you Mg. **Kaspars Pudzs** for thermoelectric measurements. Thank you Dr. **Guntis Marcins** for the training on Hall effect measurements. Thank you Dr. **Laima Trinklere** and Dr. **Valdis Korsaks** for the possibility to measure the visible light transmittance and reflection. Thank you Mg. **Karlis Kundzins** and Dr. **Krisjanis Smits** for electron microscopy images.

Thanks to **family** and **friends** for the support and patience during the development of the doctoral thesis.

Thanks the **CCEBB projects**, **LCS grant 402/2012** and **EUROfusion project CfP-WP15-ENR-01 / UL-01** for the funding.